# Compact Omnidirectional Millimeter-Wave Antenna Array Using Substrate Integrated Waveguide Technique and Efficient Modeling Approach

By

**Yuanzhi Liu**

A thesis presented to the Ottawa-Carleton Institute for Electrical and Computer Engineering in partial fulfillment to the thesis requirement for degree of

**MASTER OF APPLIED SCIENCE**

**in**

**ELECTRICAL AND COMPUTER ENGINEERING**

uOttawa

University of Ottawa
Ottawa, Ontario, Canada

March 2021

# Abstract

In this work, an innovative approach for effective modeling of substrate integrated waveguide (SIW) devices is firstly proposed. Next, a novel substrate integrated waveguide power splitter is proposed to feed antenna array elements in series. This feed network inherently provides uniform output power to eight quadrupole antennas. More importantly, it led to a compact configuration since the feed network can be integrated inside the elements without increasing the overall array size. Its design procedure is also presented.

Then, a series feed network was used to feed a novel compact omnidirectional antenna array. Targeting the 5G 26 GHz mm-wave frequency band, simulated results showed that the proposed array exhibits a broad impedance bandwidth of 4.15 GHz and a high gain of 13.6 dBi, which agree well with measured results. Its attractive features indicate that the proposed antenna array is well suitable for millimeter-wave wireless communication systems.



Keywords: modeling, substrate integrated waveguide, power splitter, antenna array, series, quadrupole, omnidirectional, 5G, high gain, millimeter-wave.

# Acknowledgements

First of all, I have to thank my parents, who always trust and support me. Thank you both for giving me strength to chase my dreams. My grandparents, girlfriend, and brother also deserve my wholehearted thanks.

I would like to express my deepest appreciation to Dr. Mustapha C.E. Yagoub and Dr. Derek McNamara. They both are very knowledgeable, kind, experienced, and patient professors. Dr. Yagoub, as my supervisor, is always trying his best to provide me with opportunities, which are valuable and helpful to build my future career. His guidance, encouragements, and insightful feedback pushed me to sharpen my thinking and improve the work. Dr. McNamara is an expert in applied and computational electromagnetics. I can gain a lot from every discussion with him. His help and suggestions through out my research brought my work to a higher level.

I would like to also extend my sincere thanks to Dr. Aldo Petosa, to the coordinator of our laboratory Mr. Alain Hénaff, and to my friends Mr. Mohammed Nassor and Mr. Mohammad Faridani for their helpful discussions and insightful suggestions.

Beside people who helped me with this work, from the bottom of my heart I am deeply indebted to all of them, including professors of my undergraduate university and my friends from China and Canada, who have always been supportive and kind to me.

# Contents

# List of Tables

# List of Figures

# List of Symbols

| | |
|---|---|
| $A$ | Auxiliary vector potential function |
| $AR$ | Axial ratio |
| $BW$ | Bandwidth |
| $D$ | Directivity |
| $\boldsymbol{E}$ | Electric field intensity |
| $FBW$ | Fractional bandwidth |
| $f_H$ | High cut-off frequency |
| $f_L$ | Low cut-off frequency |
| $G$ | Gain |
| $\boldsymbol{H}$ | Magnetic field intensity |
| $\boldsymbol{I}$ | Electric current |
| $K$ | Wave number |
| $P$ | Power |
| $P_{rad}$ | Power radiated |
| $R_{rad}$ | Radiation resistance |
| $tan\delta$ | Loss tangent |
| $U$ | Radiation intensity |
| $W_{ave}$ | Average power density |
| $\varepsilon_r$ | Relative permittivity |
| $\eta$ | Wave impedance |
| $\lambda_0$ | Wavelength in free space |
| $\lambda_g$ | Guide wavelength |
| $\mu_r$ | Relative permeability |

# List of Acronyms

| | |
|---|---|
| 3D | 3-Dimentional |
| 5G | Fifth-generation |
| AM | Amplitude modulation |
| BI-RME | Boundary Integral-Resonant Mode Expansion |
| BWFN | Beam width between first nulls |
| CST | Computer Simulation Technology |
| EM | Electromagnetic |
| FBR | Front-to-back ratio |
| HFSS | High frequency structure simulator |
| HPBW | Half power beam width |
| IEEE | Institute of Electrical and Electronics Engineers |
| ITU | International Telecommunication Union |
| LSIW | Long substrate integrated waveguide |
| Mm-wave | Millimeter-wave |
| PEC | Perfect electric conductor |
| RF | Radio frequency |
| RWG | Rectangular waveguide |
| SIW | Substrate integrated waveguide |
| SLL | Sidelobe level |
| TE | Transverse electric |
| TEM | Transverse electromagnetic |
| TM | Transverse magnetic |

# Chapter 1. Introduction

## 1.1 Background and Motivation

### 1.1.1 Importance of antennas

The official IEEE definition of an antenna, as given by Stutzman and Thiele, is “That part of a transmitting or receiving system that is designed to radiate or receive electromagnetic (EM) waves” [1]. This function of antennas makes them essential parts of any wireless system. Many types of antennas including wire antennas, apertures, lenses, printed antennas, and dielectric antennas, have been presented in the past dozens of years due to the progress of wireless communications. Classified by different physical attributes, EM behaviours, polarization …, there are plenty of classes of antennas suitable for different applications.

### 1.1.2 Millimeter-wave systems

The rapid development of wireless communication technologies has changed our lives in all aspects including transportation, shopping, communication, etc. Meanwhile, it has led to a dramatic increase in the data traffic of wireless networks [2]. To address such a challenge, the millimeter-wave spectrum has been recognized as a key technology in the future communication systems [3], [4]. In fact, it can use enormous underutilized bands beyond the traditional licensed bands and can meet the demand of high-speed transmission with remarkably increased data transmission rates compared to the lower frequency bands [5]. To this aim, the International Telecommunication Union (ITU) has licensed several mm-wave bands for the fifth-generation (5G) communications and beyond applications, including 24.25-27.5 GHz, 37-40 GHz, and 66-76 GHz [6], [7].

Despite their potential, mm-wave communication systems have an inherent shortage. According to the Friis’ transmission equation, the signal path loss between the feed points of two isotropic antennas in free space grows with the square of the frequency [8], indicating that the path loss in mm-wave bands is much higher than that of lower frequencies. Fortunately, the smaller wavelength of mm-wave signals enables proportionally greater antenna gain for the same physical antenna size [9]. For the convenience of controlling radiation pattern and input impedance, instead of designing a single antenna with remarkably increased size, antenna arrays are widely used in mm-wave applications.

### 1.1.3 Directional and omnidirectional antennas

Antennas can be classified into three categories, based on the type of patterns they produce [10]:

i) isotropic antenna: a hypothetical point source that produces a pattern that has a constant radiation intensity in all directions.

ii) omnidirectional antenna: an antenna that has a non-directional radiation pattern in azimuth and a directional pattern in elevation.

iii) directional antenna: an antenna that radiates (or receives) waves more effectively in some directions rather than in others, producing a directional radiation pattern.

Omnidirectional antennas are preferred in places like gymnasiums, malls, and offices, where potential users are evenly distributed in spacious areas [7]. This research focuses on designing a mm-wave omnidirectional antenna array.

## 1.2 Research objectives

The main objective of this research is to design a mm-wave omnidirectional antenna array with compact size and simple geometry. The array should have a relative high gain to deal with the high path loss in mm-wave bands. The starting point is designing a single omnidirectional antenna element, then finding a way to properly feed the array consists of several elements. Such a feed network should have a novel configuration since existing conventional feed networks cannot feed omnidirectional arrays without degrading the expected omnidirectional radiation pattern (which we will discuss next).

Besides, fabrication tolerance usually will cause non-consistency between simulated and measured results, especially in terms of return loss, a critical parameter that decides if the antenna can work in the targeted band(s). Therefore, this research will target at designing a broadband antenna array. Some other parameters such as side lobe levels (SLLs) and cross-polarization levels are also under consideration. Based on the specifications of the 5G 26 GHz mm-wave band [6], the specifications of the targeted design are as follows:

Type of radiation pattern: omnidirectional

Operating frequency: 26 GHz

Impedance bandwidth: > 2 GHz

Gain: > 10 dBi

Efficiency: > 80 %

## 1.3 Bottlenecks

If one plans to design an omnidirectional antenna, the first design that can come to mind will be probably related to dipole antennas since they are the simplest and most widely used class of antennas with an omnidirectional radiation

pattern [11]. In fact, some omnidirectional antennas based on dipoles have been proposed in recent years [12]-[15]. However, the gain of dipoles is low, e.g., half-wave dipoles have a theoretical gain of only 2.15 dBi. Enlarging the length of a dipole can of course improve its gain, but it is usually difficult to control its side lobe levels [16]. So, to improve its gain, one would prefer to design an array.

However, the existence of the feed network can significantly degrade the omnidirectional radiation pattern of the dipoles because the ground of the feed network can work as a reflector [17]. No matter the kind of antenna elements used, one must address such a challenging issue to design an omnidirectional antenna array. In fact, even for single antennas, only few mm-wave omnidirectional works have been reported. In [18], an omnidirectional antenna operating at 28 GHz is presented; although it has a complex non-planar structure, a small gain of 2.08 dBic, and a narrow -10 dB impedance bandwidth (27 - 28.5 GHz, 5.4%). The planar antenna presented in [19] achieved a better performance in bandwidth (57 - 64 GHz, 11.6%), but its average gain is only 1.4 dBi.

## 1.4 Research contributions

In this research, the well-known substrate integrated waveguide (SIW) technique [20] has been adopted to design a novel series feed network and thus building an omnidirectional antenna array. SIW has many superior features. It can be directly and easily integrated with planar circuits compared to conventional waveguides since it is in fact a planar form of waveguide. Besides, compared to microstrip lines, it generally has lower losses and much less undesired power radiations at high frequencies such as mm-wave bands [21], [22]. Also considering its simple fabrication process, low cost compared to conventional waveguide devices, the SIW technique has been chosen as a candidate for this research.

Different original contributions can be highlighted:

- An enhanced approach for efficient modeling of SIW structures in 3D-EM simulators such as High Frequency Structure Simulator (HFSS) and Computer Simulation Technology (CST) is proposed at first. The approach replaces the complicated structure of SIW by a surrogate model, which allows to easily and efficiently optimize the SIW circuits, in particular, and any device under design, in general.
- Next, a new omnidirectional printed antenna configuration namely, a quadrupole, is introduced. Such antenna consists of two dipoles and a power splitter inside them for feeding. The attractive features of dipoles are maintained, and the gain is enhanced.
- Then, a long SIW (LSIW) feed network, which can inherently provide uniform output power to antenna elements, is proposed. In fact, even if the SIW technique has been widely used in a large variety of circuits [23]-[27], existing SIW power splitters designed for feeding antenna arrays are based on parallel feeding topologies. Such a feed network has been adopted to feed eight quadrupole antennas. It leads to a compact configuration since the feed network can be integrated inside the elements without increasing the array size. Its design procedure is also presented.

- Finally, the LSIW series feed network was used to feed a novel compact omnidirectional antenna array. Targeting the 5G 26 GHz mm-wave band, simulated results show that the array has a high gain of 13.6 dBi, a broad impedance bandwidth of 4.15 GHz (fractional bandwidth of 17%) for $|S_{11}| < -10$ dB. It also has a high efficiency and low cross-polarization levels at two principle planes (E-plane and H-plane). A prototype was fabricated and measured; the measured return loss shows an even better impedance bandwidth of 6.71 GHz, and other results match well with the simulated results. Despite its good performance, the array features a compact size of only $62 \times 12$ mm$^2$ ($5.37\ \lambda_0 \times 1.04\ \lambda_0$, with $\lambda_0$ the free space wavelength at 26 GHz), low cost, low profile, and simple fabrication process. Its attractive features indicate that the proposed antenna array is well suitable for millimeter-wave wireless communication systems.

## 1.5 Thesis Outline

The thesis consists of seven chapters. Chapter 1 is a general introduction to the research topic. Chapter 2 introduces antenna basics and the SIW technique. Chapter 3 presents the surrogate model of SIW structures. Chapter 4 presents the novel printed antenna configuration namely, the quadrupole antenna.

Chapter 5 presents the LSIW feed network. Chapter 6 presents the printed quadrupole antenna array. Finally, conclusions are drawn, and future work is discussed in chapter 7.

## 1.6 List of publications

A complete list of published/accepted papers related to the thesis is listed below:


[1] **Y. Liu**, M.C.E. Yagoub, "Compact Omnidirectional Millimeter-Wave Antenna Array Fed in Series by a Novel Feed Network", *IEEE Transactions on Antennas and Propagation*, accepted.

[2] **Y. Liu**, M.C.E. Yagoub, "Compact, Broadband, and Omnidirectional Antenna Array for Millimeter-Wave Communication Systems", *Journal of Microwaves, Optoelectronics and Electromagnetic Applications*, 2021.

[3] **Y. Liu**, M.C.E. Yagoub, "Wideband millimeter wave planner sub-array with enhanced gain for 5G communication systems", *IEEE MTT-S International Conference on Numerical Electromagnetic and Multiphysics Modeling and Optimization*, 2020.

[4] **Y. Liu**, M. Faridani, and M.C.E. Yagoub, "Compact Wideband Linear Antenna Array Using Substrate Integrated Waveguide Cavity for 5G Communication Systems", *IEEE MTT-S International Conference on Numerical Electromagnetic and Multiphysics Modeling and Optimization*, 2020.

[5] **Y. Liu**, G. Bai, and M.C.E. Yagoub, "A 79GHz Series Fed Microstrip Patch Antenna Array with Bandwidth Enhancement and Sidelobe Suppression", *International Conference on Radar, Antenna, Materials, Electronics and Telecommunications*, 2020.

[6] **Y. Liu**, M.C.E. Yagoub, M. Nassor, "Omni-directional Antenna Array with Improved Gain for 5G Communication Systems", *IEEE International Symposium on Antennas and Propagation and North American Radio Science Meeting*, 2020.

# Chapter 2. Antenna Fundamentals and Adopted Techniques

## 2.1 Antenna basics

As stated previously, antennas are essential for any wireless systems. They can be designed to operate over a wide range of frequencies, from kilohertz (such as AM radio broadcast antennas) to terahertz and beyond (for emerging applications such as medical imaging) [10].

Antennas can be characterized by specifying various electrical parameters. The most important of these are summarized in this section.

### 2.1.1 Radiation patterns

The radiation pattern of antennas refers to the directional (angular) dependence of the strength of the radio waves from the antenna or other source [28]. It is usually specified in the far field region, i.e., far enough away from the antenna such that the angular field distribution is essentially independent of distance.

As discussed, there are three types of radiation patterns namely, isotropic, omnidirectional, and directional. The radiation patterns of antennas are 3-Dimensional. However, to easily describe an antenna's radiation performance, designers always use two principle plane cuts containing the E-plane and H-plane patterns. The E-plane is the plane containing the electric field vector and the direction of maximum radiation while the H-plane is the plane containing the magnetic field vector and the direction of maximum radiation. These two planes are always orthogonal [10].

The radiation pattern of a directional antenna might consist of several lobes. These lobes can be divided into the main lobe and minor lobes. The main lobe is the one containing the direction of maximum radiation, while the minor lobes are all the other lobes. Side lobes are minor lobes adjacent to the main lobe, while the back lobe is the lobe directly opposite the main lobe. There are several terminologies to describe a directional radiation pattern [10]:

i) The half power beam width (HPBW), also called 3 dB beam width, is the angle in which the radiation intensity is greater than one-half of the maximum value of the main lobe.

ii) The beam width between first nulls (BWFN) is the angle between the first nulls on either side of the main beam. Not all radiation patterns will have nulls in some or all of the pattern cuts.

iii) The maximum relative side lobe level (SLL) is the ratio of the power in the highest sidelobe to the power in the main lobe. Usually, this ratio should be as low as possible since it is desirable to focus as much energy as possible into the main lobe.

iv) The front-to-back ratio (FBR) is the ratio of the power in the main lobe to the power in the back lobe. For most applications, this ratio should be as high as possible, to minimize unwanted energy in the back lobe.

### 2.1.2 Directivity and gain

Directivity of an antenna is a measure of the amount of energy concentrated in the main beam of an antenna pattern. The directivity *D* of an antenna is equal to the ratio of the radiation intensity in a given direction over that of an isotropic source [10].

Gain of an antenna is closely associated with its directivity. This parameter takes any losses within the antenna into account. Antenna gain *G* can be calculated by:

$$G = e_{rad} D \tag{2.1}$$

where $e_{rad}$ is the antenna radiation efficiency, a measure of how much of the power entering the antenna is radiated and it accounts for conduction and dielectric losses in the antenna.

### 2.1.3 Bandwidth

The bandwidth *BW* of an antenna refers to the range of frequencies over which the antenna can operate satisfactorily. Two main factors are commonly of interest for antenna design [10]:

i ) Input Impedance Bandwidth: The impedance presented by the antenna at its input terminal changes with frequency. The antenna can only accept (or deliver) power to the transmission guide when its input impedance is matched to the impedance of the guide. Outside this frequency the antenna will reflect the incident power and will not radiate (or receive) EM waves.

ii ) Pattern Bandwidth: Various radiation pattern parameters, e.g., gain, beam widths, side lobe levels, are a function of frequency. The pattern bandwidth will be determined by the range of frequencies over which one or more of these parameters meets certain required specifications.

The bandwidth *BW* is calculated by the difference between the upper frequency $f_H$ and lower frequencies $f_L$, which refers to the absolute bandwidth:

$$BW = f_H - f_L \tag{2.2}$$

However, the absolute bandwidth in the field of antennas is not always the most appropriate or useful measure of bandwidth. For example, the challenge of constructing an antenna to meet a specified absolute bandwidth is easier at

a higher frequency than at a lower frequency [29]. For this reason, the fractional bandwidth (*FBW*), which can give a better indication of performance of the antenna, is often used. It is given by:

$$FBW = BW / f_0 \times 100\% \tag{2.3}$$

where $f_0$ is the center frequency of the antenna.

### 2.1.4 Polarization

The polarization of an EM wave describes the time-varying direction and relative magnitude of the electric field vector. If the time-varying electric field is represented by a vector, the polarization of the wave can be thought of as the locus traced by the tip of this vector in time, at a fixed position in space. The sense of polarization is defined as being observed in the direction of propagation. The polarization of an antenna is defined as being the same as the polarization of a wave transmitted by that antenna. In the most general case, a plane wave will have an elliptical polarization. In other words, at a fixed point in space, the magnitude of the electric field will trace out an ellipse. Defining the major axis of the ellipse as *a* and the minor axis as *b*, the ratio of the two is known as the axial ratio [10]:

$$AR = a / b \tag{2.4}$$

In the particular case where $b = 0$, $AR = \infty$. This case is the so-called linear polarization case, and the wave is referred to be linearly polarized. While when $a = b$, $AR = 1$, the wave is circularly polarized. For circular polarization, the sense of polarization can be categorized as either clockwise (right-hand) or counter clockwise (left-hand) as observed along the direction of propagation. Note that researchers in different research areas may have opposite answers for the circular type of a same wave.

## 2.2 Dipole antennas

Printed dipoles are used as radiation parts in this research work. So, this section introduces some theoretical analysis for the infinitesimal dipole and finite-length dipole.

### 2.2.1 Analysis of the infinitesimal dipole

Linear wire antennas are probably the simplest and most widely used class of antennas in radio and telecommunications. To have a basic understanding of this type of antenna, it is instructive to first investigate on the case of an infinitesimal dipole [10], as shown in Fig. 2.1.

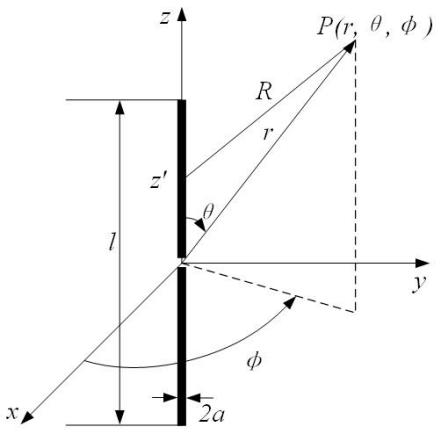

Fig. 2. 1. Infinitesimal dipole ($l$, $a << \lambda$).

In this figure, the infinitesimal dipole, oriented parallel to the $z$-axis, consists of a wire whose length $l$ and radius $a$ are very small compared to the wavelength of operation. Since the length of the wire is so small, the electric current along the wire then can be assumed to be constant and flowing solely in the $z$-direction [10]:

$$\boldsymbol{I}\left(x',y',z'\right)=I_0\hat{\boldsymbol{z}} \tag{2.5}$$

The auxiliary vector potential function is given by:

$$A\left(x,y,z\right)=\frac{\mu}{4\pi}\int_{-l/2}^{l/2} I\left(x',y',z'\right)\frac{e^{-jkR}}{R}dl' \tag{2.6}$$

where $R$ is given by:

$$R=\sqrt{\left(x-x'\right)^2+\left(y-y'\right)^2+\left(z-z'\right)^2} \tag{2.7}$$

But for the infinitesimal dipole, we have $x' = y' = z' = 0$, so that (3.7) reduces to:

$$R=\sqrt{x^2+y^2+z^2}=r \tag{2.8}$$

Substituting (2.5) and (2.8) into (2.6) and carrying out the integration over the length of the infinitesimal dipole, gives the following result:

$$\boldsymbol{A}\left(x,y,z\right)=\frac{\mu I_0 l}{4\pi}\frac{e^{-jkr}}{r}\hat{\boldsymbol{z}} \tag{2.9}$$

Therefore, in the far-field region, the fields are:

$$\begin{aligned} H_\phi &\approx \frac{jkI_0 \sin\theta}{4\pi}\frac{e^{-jkr}}{r} \\ E_\theta &\approx \frac{j\eta kI_0 \sin\theta}{4\pi}\frac{e^{-jkr}}{r} \\ H_r &= H_\theta = E_r = E_\phi = 0 \end{aligned} \tag{2.10}$$

The complex power of the infinitesimal dipole moving in the radial direction can be calculated by:

$$P = \int_0^{2\pi}\int_0^{\pi}\left(\frac{1}{2}\boldsymbol{E}\times\boldsymbol{H}^*\cdot\hat{\boldsymbol{r}}\right)r^2\sin\theta d\theta d\phi = \eta\frac{\pi}{3}\left|\frac{I_0 l}{\lambda}\right|^2\left[1-j\frac{1}{(kr)^3}\right] \tag{2.11}$$

Then, the radiated power is:

$$P_{rad} = \eta\frac{\pi}{3}\left|\frac{I_0 l}{\lambda}\right|^2 \tag{2.12}$$

and the radiation resistance is:

$$R_{rad} = 80\left(\frac{\pi l}{\lambda}\right)^2 \tag{2.13}$$

The average power density of the infinitesimal dipole is given by:

$$\boldsymbol{W}_{ave} = \frac{1}{2}\mathrm{Re}\left(\boldsymbol{E}\times\boldsymbol{H}^*\right) = \hat{\boldsymbol{r}}\frac{\eta}{2}|I_0|^2\left(\frac{kl\sin\theta}{4\pi r}\right)^2 \tag{2.14}$$

from which the radiation intensity can be calculated by:

$$U = r^2\boldsymbol{W}_{ave} = \frac{\eta}{2}|I_0|^2\left(\frac{kl\sin\theta}{4\pi}\right)^2 \tag{2.15}$$

The maximum directivity of the dipole can then be determined using:

$$D = 4\pi\frac{U_{\max}}{P_{rad}} = \frac{\frac{\eta}{2}|I_0|^2\left(\frac{kl}{4\pi}\right)^2}{\frac{\eta\pi}{3}|I_0|^2\left(\frac{l}{\pi}\right)^2} = \frac{3}{2} \tag{2.16}$$

## 2.2.2 Analysis of the finite-length dipole

There is no infinitesimal dipole antenna in practice. So, to solve the radiated fields for a dipole with a finite length, the following steps can be carried out [10].

The finite-length dipole shown in Fig. 2.2 is oriented parallel to the *z*-axis. It consists of a wire whose length is *l* and radius is *a*. The dipole is very thin so that *a* is negligible compared to the wavelength.

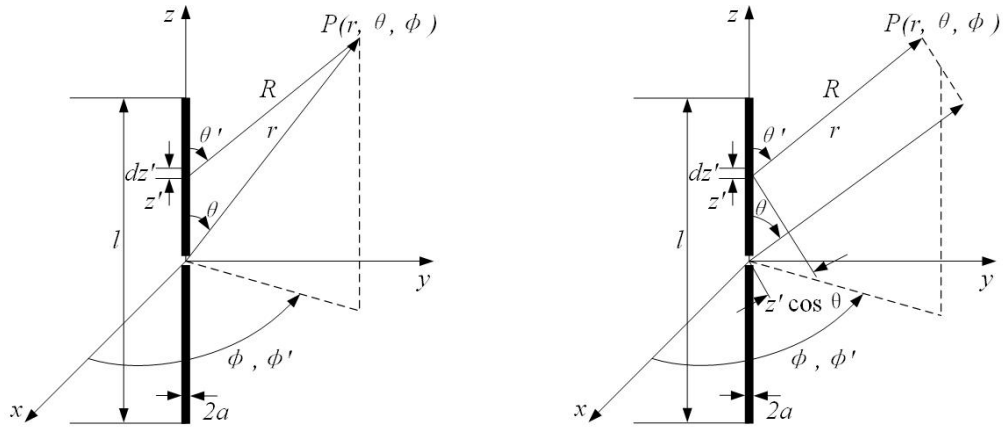


a. b.

Fig. 2. 2. Finite-length dipole antenna and its far-field approximation (a. finite-length dipole antenna; b. far-field approximation).

The current is not uniform over the length. Instead, for a very thin dipole, the current $\boldsymbol{I}$ along the wire can be approximated by the following formulae [10]:

$$\boldsymbol{I}(x',\,y',\,z')=\begin{cases}\hat{\boldsymbol{z}}\cdot I_0\sin\left[k\left(\dfrac{l}{2}-z'\right)\right],\ 0\le z'\le\dfrac{l}{2}\\ \hat{\boldsymbol{z}}\cdot I_0\sin\left[k\left(\dfrac{l}{2}+z'\right)\right],\ 0\le z'\le\dfrac{l}{2}\end{cases}\tag{2.17}$$

where $I_0$ is a constant. This current distribution assumes that the dipole is center fed and that the current vanishes at the end points. The distance $R$ from a point $z'$ to the observation point $P$ (Fig. 2. 2.b) can be expressed as:

$$R=\sqrt{x^2+y^2+\left(z-z'\right)^2}\tag{2.18}$$

In the far-field region of the dipole ($R >> 2l^2/\lambda$), as shown in Fig. 2.2.b, the following approximations can be made to determine the radiation patterns:

$$\begin{aligned}&R\approx r, && \text{for amplitide terms}\\ &R\approx r-z'\cos\theta, && \text{for phase tems}\end{aligned}\tag{2.19}$$

The dipole can be considered as a set of infinitesimal dipoles of length *dz'*, each positioned along the *z*-axis at *z'*. Each infinitesimal dipole will make a contribution to the far-fields $dE_\theta$ and $dH_\varphi$ as expressed below:

$$\begin{aligned} dE_\theta &\approx \frac{j\eta kI(z')\sin\theta}{4\pi}\frac{e^{-jkR}}{R}dz' \\ dH_\varphi &\approx \frac{jkI(z')\sin\theta}{4\pi}\frac{e^{-jkR}}{R}dz' \end{aligned} \tag{2.20}$$

and using the far-field approximation from (2.19), the fields become:

$$\begin{aligned} dE_\theta &\approx \frac{j\eta kI(z')\sin\theta}{4\pi}\frac{e^{-jk(r-z'\cos\theta)}}{r}dz' \\ dH_\varphi &\approx \frac{jkI(z')\sin\theta}{4\pi}\frac{e^{-jk(r-z'\cos\theta)}}{r}dz' \end{aligned} \tag{2.21}$$

The total fields are then obtained by integrating over the length of the dipole:

$$\begin{aligned} E_\theta &= \int_{-l/2}^{l/2} dE_\theta = \frac{j\eta k\sin\theta e^{-jkr}}{4\pi r}\int_{-l/2}^{l/2} I(z')e^{jkz'\cos\theta}dz' \\ H_\varphi &= \int_{-l/2}^{l/2} dH_\varphi = \frac{jk\sin\theta e^{-jkr}}{4\pi r}\int_{-l/2}^{l/2} I(z')e^{jkz'\cos\theta}dz' \end{aligned} \tag{2.22}$$

Substituting for *I* from (2.17) into (2.22), the total fields in the far-field region of the finite-length dipole can be determined:

$$\begin{aligned} E_\theta &= \frac{j\eta I_0 e^{-jkr}}{2\pi r}\left[\frac{\cos\left(\frac{kl}{2}\cos\theta\right)-\cos\left(\frac{kl}{2}\right)}{\sin\theta}\right] \\ H_\varphi &= \frac{jI_0 e^{-jkr}}{2\pi r}\left[\frac{\cos\left(\frac{kl}{2}\cos\theta\right)-\cos\left(\frac{kl}{2}\right)}{\sin\theta}\right] \end{aligned} \tag{2.23}$$

The time average Poynting vector of the finite-length dipole is given by:

$$\boldsymbol{W}_{ave} = \frac{1}{2}\mathrm{Re}\left(\boldsymbol{E}\times\boldsymbol{H}^*\right) = \hat{\boldsymbol{r}}\frac{\eta}{8}|I_0|^2\left[\frac{\cos\left(\frac{kl}{2}\cos\theta\right)-\cos\left(\frac{kl}{2}\right)}{\pi r\sin\theta}\right]^2 \tag{2.24}$$

so that the radiation intensity:

$$U = r^2 \boldsymbol{W}_{ave} = \frac{\eta}{8}|I_0|^2 \left[ \frac{\cos\left(\frac{kl}{2}\cos\theta\right) - \cos\left(\frac{kl}{2}\right)}{\pi r \sin\theta} \right]^2 \tag{2.25}$$

The normalized radiation patterns of the dipole with various lengths are plotted in Fig. 2.3. As the length of the antenna increases, the beam narrows and thus, the directivity increases. When the length of the dipole exceeds a wavelength, additional lobes will appear in the radiation pattern [10].

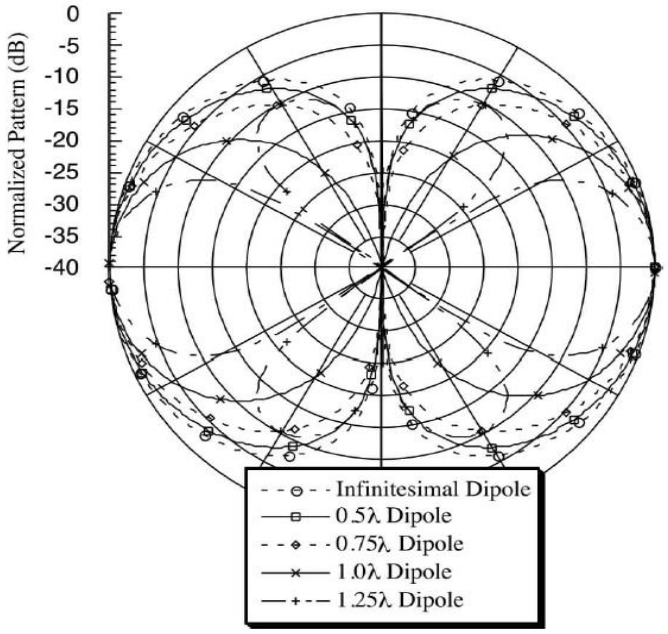


Fig. 2. 3. Radiation patterns of dipoles with various lengths [10].

## 2.3 Substrate integrated waveguide technique

The SIW technique was first reported more than twenty years ago [20]. Composed of two rows of metallized via holes embedded in a dielectric substrate that connect two parallel metal plates, a planar form of rectangular waveguide (Fig. 2.4) filled with dielectric material is constructed, allowing a complete integration with other planar circuits [30]. Since then, a large variety of SIW-based devices such as filters, antennas, power splitters and so on have been designed [23]-[27] because SIW offers several attractive features such as high power capacity, low cost, and low profile [30].

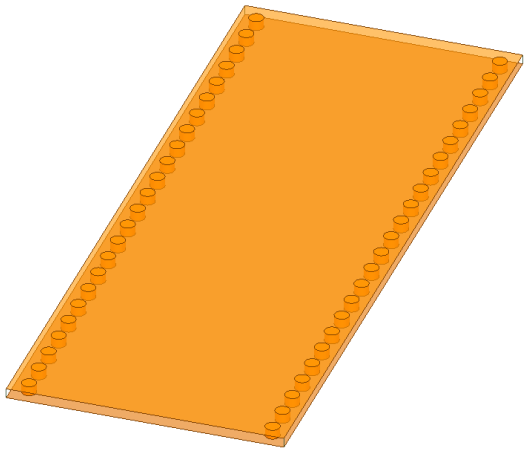

Fig. 2. 4. Substrate integrated waveguide.

## 2.4 Conclusion

Some antenna basics were discussed in this chapter. The concepts of radiation patterns, directivity, gain, efficiency, bandwidth, and polarization were mainly focused on since these parameters are directly linked to this research.

Dipole antennas were used in this research, thus the radiation characteristics of dipoles including infinitesimal one and finite-length one were analyzed. The chapter also briefly introduced the SIW technique.

Although this technique has been widely adopted in the field of RF and microwave, and the electrical characteristics of SIWs have been comprehensively analyzed, SIW structures cannot be optimized directly and easily. This issue has been handled by an approach proposed in this research work, which will be discussed in the next chapter.

# Chapter 3. Surrogate Model of SIW

As previously mentioned, SIW technique has been widely implemented in RF engineering. However, unlike other simple structures such as microstrip lines whose characteristic impedance, guide wavelength, etc. can be precisely calculated according to empirical equations, or rectangular waveguides (RGWs) which have several standards set by different countries so that one can choose a standard size according to the targeted applications, designing an SIW-based circuit or device is complicated. A very basic SIW has at least six physical parameters that affect its characteristics [31], namely its physical length $L_s$ and width $W_s$, permittivity $\varepsilon_r$ and height $h$ of the substrate, diameter of via holes $d$, and space of adjacent via holes $p$. Besides, extra transitions such as tapered microstrip-to-SIW transitions and coplanar feedings are usually needed to feed SIWs [32], making develop comprehensive equations to calculate physical parameters precisely before design like what we can do with microstrip lines even more unrealistic.

Fortunately, we do not need to. Thanks to the progress of 3D-EM simulators such as *Ansys-HFSS* [33] and *CST Studio Suite* [34], engineers can design many kinds of SIW-based devices [35]-[37] by first, roughly calculating the initial values of their physical parameters using existing empirical equations and then, run an optimization loop to maximize the device performance.

## 3.1 Modeling SIW in HFSS

The modeling procedure of SIW in a commercial software like *Ansys-HFSS* is not straightforward. Fig. 3.1 shows a basic 2-port SIW structure, consisting of a SIW and two microstrip-to-SIW transitions. The device is printed on the Rogers RO4003C laminate with $\varepsilon_r = 3.55$, $\tan\delta = 0.0027$, substrate thickness of 0.203 mm, and conductor thickness of 0.035 mm (All the devices presented in this thesis were printed on this substrate). The ports 1 and port 2 are symmetric. To model the metalized via hole arrays, we need to specify the diameter of via holes $d$, space of adjacent via holes $p$, and the number of the via holes $N$. If we draw two rows of via holes along the $x$-axis, as illustrated in Fig. 3.1, we have

$$L_s = (N-1)p \tag{3.1}$$

where $L_s$ is the physical length of SIW. In the most general case, we first calculated how many vias we need using (3.1). Next, we drew a via hole array consisting of $N$ metalized via holes. However, since the values of the parameters are just initial values, the values need to be adjusted to get expected performance; optimization round is necessary. The final optimized geometrical values for a cut-off frequency around 18 GHz are given in Table 3.1.

In such design, the parameters of the vias are interlinked such that any change in one value might cause significant alteration of the global SIW response. The optimization process consists of varying one parameter at a time, while keeping the others fixed. This is not so forthright because vias cannot be duplicated/removed automatically during the optimization routine. Therefore, the number of vias cannot be routinely adjusted during the optimization loop.

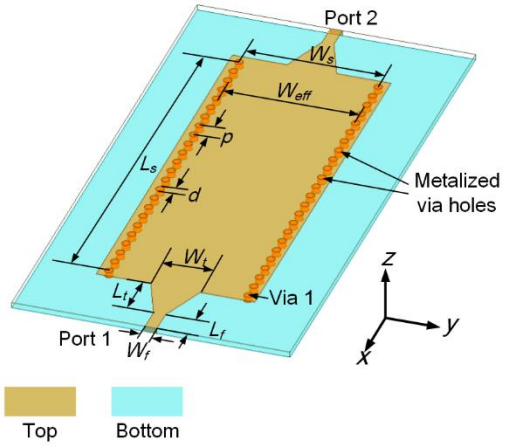


Fig. 3. 1. An SIW configuration.

Table 3. 1. Parameters of the SIW

| Parameters | Value (mm) | Parameters | Value (mm) |
|---|---|---|---|
| $W_f$ | 0.4260 | $L_f$ | 0.9125 |
| $W_t$ | 1.7800 | $L_t$ | 1.7375 |
| $p$ | 0.6087 | $d$ | 0.3000 |
| $W_s$ | 5.0000 | $L_s$ | 14.0000 |

In this design, we set the number of vias to $N$ = 24. From that, we can see in Fig. 3.2 some unrealistic structures while varying $p$. In Fig. 3.2.a, the original SIW part became shorter since the space of adjacent vias have been decreased while the number of vias was not varied since they could not be automatically increased accordingly. Similarly, in Fig. 3.2.b, some vias have been replaced out of the original SIW part since the number of vias could not be decreased simultaneously as well. In Fig. 3.2.c, the model even become invalid. Therefore, we have to manually redraw the structure after each iteration while varying $p$.

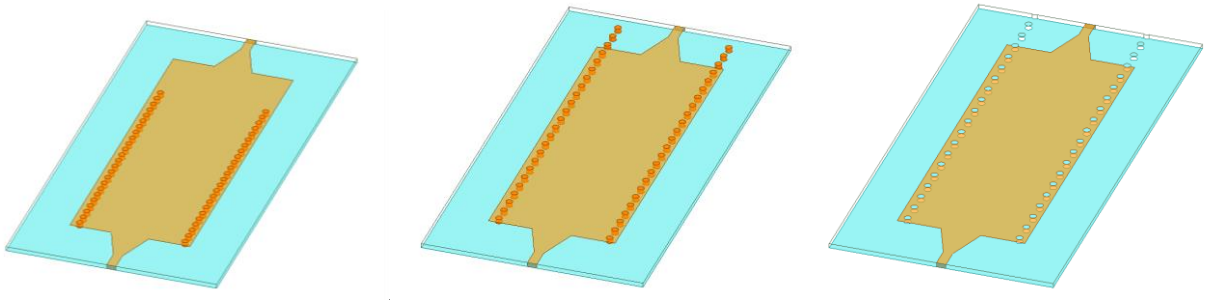

a. b. c.

Fig. 3. 2. The SIW structure changes with the change of $p$ while other parameters are fixed ($L_s$ = 14 mm, $d$ = 0.3000 mm, $N$ = 24), (a. $p$ = 0.5 mm, b. $p$ = 0.7 mm, and c. $p$ = 0.9 mm).

As for the SIW length $L_s$, which is also a critical parameter to determine the operating frequencies of the SIW if it is in the order of the SIW width $W_s$ (we will discuss it in the next section), we can get similar unworkable behaviours. Fig. 3.3 shows the SIW structures with different $L_s$. Because the number of vias could not change accordingly, simply optimizing the SIW length will also cause the deformation of the structure.

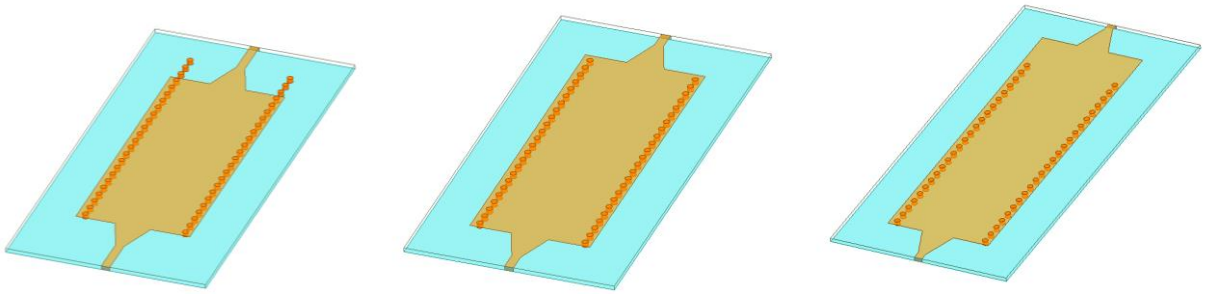

a. b. c.

Fig. 3. 3. The SIW structure changes with the change of $L_s$ while other parameters are fixed ($d$ = 0.3000 mm, $p$ = $L_s/(N\text{-}1)$, $N$ = 24), (a. $L_s$ = 12 mm, b. $L_s$ = 14 mm, and c. $L_s$ = 16 mm).

To avoid such kind of issues, instead of defining every necessary parameters, one can set $L_s$ to be changed with the change of $p$, or set $p$ to be changed with the change of $L_s$, that is, following (3.1) to define variables. In this case, when one parameter is under optimization, at least the other will change accordingly and the SIW structure will not get deformed ideally. For example, if we set $p$ always equals to $L_s/(N\text{-}1)$ (with $N$ = 24 in this design), $p$ will change when $L_s$ changes. Fig. 3.4 shows the structure of the SIW with different $L_s$. Obviously, this time the SIW did not get deformed, at least optimization can be run even though we cannot let $L_s$ to be too small or too large compared to the initial value, since the vias will either overlap or be too far from adjacent ones (power leakage will be significant and the SIW will not work).

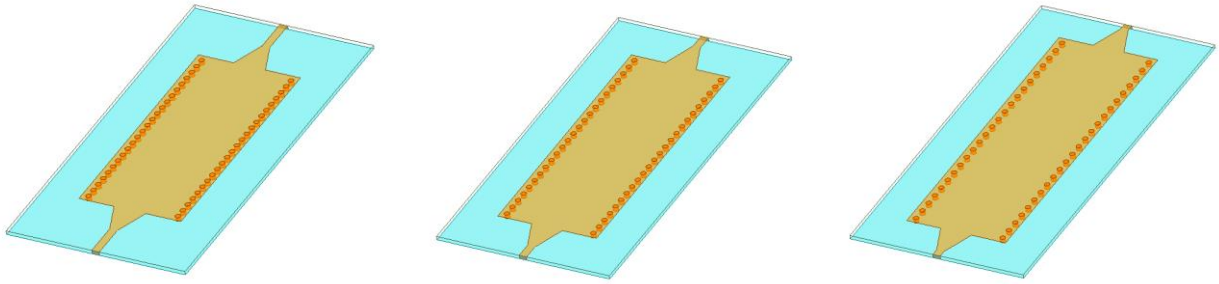

a. b. c.

Fig. 3. 4. The SIW structure changes with the change of $L_s$ while other parameters are fixed ($d$ = 0.3000mm, $p$ = $L_s/(N\text{-}1)$, $N$ = 24), (a. $L_s$ = 12 mm, b. $L_s$ = 14 mm, and c. $L_s$ = 16 mm).

However, recall that this is just a very simple SIW structure, SIW devices such as filters, power splitters, and antennas will never be so simple. They will contain some gaps, other structures, or even more than one layers. Therefore, it is always very difficult to optimize an SIW device, manually adjusting the model is needed at most of the time.

## 3.2 SIW design approaches

Instead of trying to optimize a physical SIW structure directly in a commercial software, a new approach is proposed in this chapter. This approach allows one to easily optimize an SIW structure without manually justifying the model. And thus, the design process will be simplified, and a lot of time saved. This approach is based on some fundamental SIW theories previously presented by other researchers.

### 3.2.1 Rectangular waveguide

Rectangular waveguides (RWGs), one of the earliest types of transmission lines, have been used in many applications [38]. They can be used to design various microwave and millimeter wave devices such as isolators, attenuators, couplers, power splitters, etc. The shape of an RWG is shown in Fig. 3.5. A material with relative permittivity $\varepsilon_r$ and relative permeability $\mu_r$ fills the inside of the conductors, which can be regarded as perfect conductor (PEC) sheets when analyzing the EM phenomenon of the RWG. A rectangular waveguide supports TM and TE modes but not TEM waves because we cannot define a unique voltage since there is only one conductor in a rectangular waveguide [38].

RWGs are simple structures that can be easily modeled and used to design devices with high Q-factor. Besides, engineers can get standard sizes of the RWG to be used based on the targeted frequencies since the RWG standard sizes have been developed internationally or domestically [39]. However, RWG devices are difficult to be integrated with planar circuits [40]. Existing planar-to-RWG transitions are bulky and need precise machining processes [41]-[44], which are difficult to achieve mass production. Furthermore, some constraints, e.g., planar substrate must be cut into a specific shape and tuning is always essential, making the integration costly and time-consuming [40].

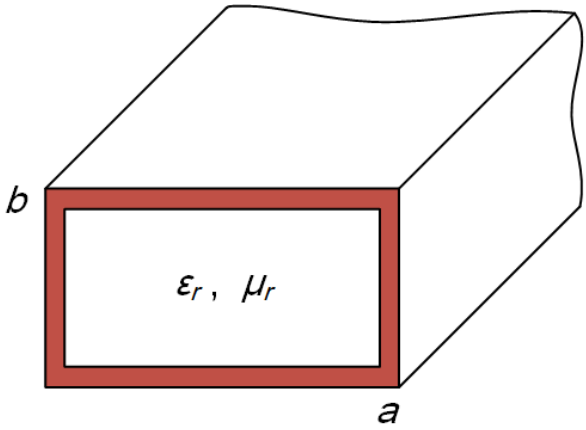


Fig. 3. 5. Rectangular waveguide.

### 3.2.2 Rectangular waveguide in planar form

To address the issues mentioned above, a planar form of rectangular waveguide was proposed by F. Shigeki in 1994 [45]. Composed of two vertical conductors that connect two parallel metal plates of substrate, a planar rectangular waveguide (Fig. 3.6) filled with dielectric material was constructed, allowing a complete integration with other planar circuits. We can see from Fig. 3.6 that this type of so-called planar RWG is just another form of RWG; its physical height is determined to be the thickness of the used dielectric substrate, and the filled material is the material of the dielectric substrate. Therefore, the planar RWG has similar EM phenomena compared to the conventional one, and such a configuration can be easily integrated with microstrip lines and other planar circuits.

However, this type of planar RWG has not been widely used in industry because its fabrication process is not simple. Instead, another form of planar RWG has been developed, which uses metalized via holes to connect upper and bottom layers of a substrate. Drilling metalized via holes is a mature technique that has been widely used in power amplifiers and some other RF/microwave circuits to raise the ground up to the same plane as the circuits. This new form of planar RWG is called the substrate integrated waveguide (refer to Fig. 3.1) [40]. In fact, the metalized via hole arrays play the same role in the waveguide as the bilateral vertical conductors shown in Fig. 3.6.

The work mechanism of the SIW has been widely investigated [46]-[49]. The surface currents are established when a mode is established in SIW that can be regarded as a special rectangular waveguide with a series of slots on the bilateral walls [49]. If the slots cut the currents, a large amount of power may be radiated. This is in fact the well-established design principle of waveguide slot antennas [50]-[52]. However, if the slots are along the direction of current flowing, there is only very little radiation [49].

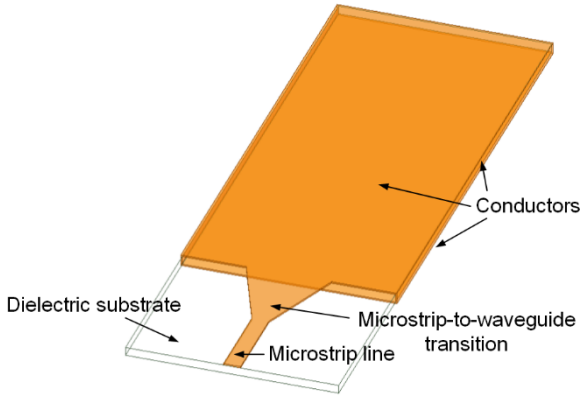


Fig. 3. 6. Rectangular waveguide in planar form.

Fig. 3.7 shows the $TE_{10}$ mode surface current flowing pattern of an SIW structure, which is similar to that of conventional RWG. The slots do not cut the surface current on the bilateral narrow walls so that the mode can be preserved. The other $TE_{m0}$ modes are similar. Therefore, $TE_{m0}$ modes can exist in SIW structures. TM modes, on the other side, will cause a large amount of power radiation since transverse magnetic field will produce longitudinal surface currents and the slots will cut these currents. Besides, $TE_{mn}$ (with *n* not being equal to zero) modes will also yield a large amount of radiation. Hence, the slot radiation suggests that only $TE_{m0}$ modes would be allowed in SIW [49]. In this case, SIW and conventional RWG have very similar behaviours.

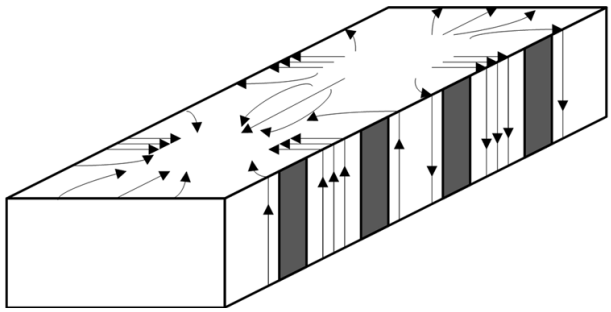

Fig. 3. 7. $TE_{10}$ surface current distribution of the SIW [49].

This is why SIW can work as a waveguide. In fact, previous researches have highlighted that an SIW can be properly designed based on the following rules [53], [54].

$$d < p \le 2d \tag{3.2}$$

$$d < \lambda_g / 5 \tag{3.3}$$

where $d$ is the diameter of the via holes, $p$ is the distance between two adjacent vias, and $\lambda_g$ is the guide wavelength of the SIW. These rules are to handle the potential power leakage problem caused by the periodic gaps on the bilateral walls.

In other words, if the gaps are too large, power leakage cannot be ignored and thus unexpected losses will be large, which will affect the SIW performance including insertion loss, impedance matching, etc. However, if $d$ and $p$ satisfy the rules, power leakage can be ignored and SIW can be regarded as a RWG to some extent, e.g., if we are talking about $TE_{mn}$ modes.

## 3.3 Surrogate model

As previously discussed, modeling and optimizing SIW structures, even very basic ones, in commercial software such as HFSS is complicated and time-consuming. Now, because basic SIWs and conventional RWGs have similar behaviours, SIWs can be probably replaced by RWGs in simulations, that is, using RWGs as surrogate models for SIWs modeling and optimization.

### 3.3.1 Physical width and length of the surrogate model

In the works of Y. Cassivi *et al*., the dispersion characteristics of SIW were analyzed using the Boundary Integral-Resonant Mode Expansion (BI-RME) method and then compared to RWGs. One conclusion they drawn was that SIWs and RWGs have the same dispersion characteristics such that SIWs are equivalent to RWGs [55]. And hence, an SIW can be analyzed as an RWG with a width of $W_{eff}$ (instead of the physical width $W_s$) while other parameters remain the same as those of the SIW. $W_{eff}$ is the then defined as the effective width of the SIW (Fig. 3.8) [55]:

$$W_{eff} = W_s - d^2/0.95p \tag{3.4}$$

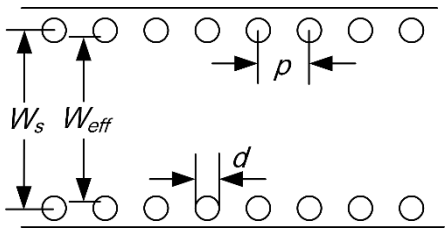


Fig. 3. 8. Top view of a basic SIW configuration.

In the existing literature, some other empirical equations have also been proposed to determine $W_{eff}$ [49], [54]. They mainly conclude that the effective width of an SIW is slightly smaller than the physical width of the SIW, and their calculated results are actually almost the same. Therefore, in this work, we retained the above relation as the most widely used and the simplest equation.

Sometimes the SIW structures can be a cavity such as that shown in Fig. 3.9. In this case, one might need its effective length $L_{eff}$ to convert it to its equivalent RWG. Similar to the effective width, the effective length of an SIW $L_{eff}$ can be calculated as function of the physical width $L_s$ of the SIW by [48]:

$$L_{eff} = L_s - d^2/0.95p \tag{3.5}$$

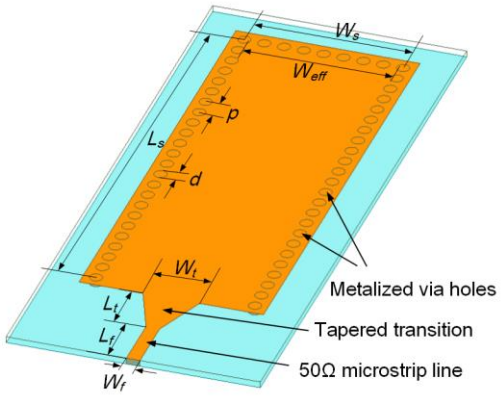


Fig. 3. 9. An SIW cavity.

The proposed surrogate model is in fact an RWG. We use PEC sheets without thickness to replace all the metalized via hole arrays in an SIW device. The PEC sheets and two conductive plates on the two sides of the substrate make such a surrogate model an RWG with a width of $W_{eff}$.

### 3.3.2 Surrogate model modeling examples and verification

We use PEC sheets to replace the metalized via holes such that the optimization issues discussed in Section 3.1 can be handled. In this part, we will use the proposed surrogate model to model some SIW structures and devices to validate the approach.

Let us consider the basic SIW structure shown in Fig. 3.1 at first. Fig. 3.10.a shows the fine model and Fig. 3.10.b the surrogate model. The effective width of the SIW is calculated to be 4.84 mm according to (3.4), so the surrogate coarse model will be an RWG with width of 4.84 mm. All other parameters are the same, and all other setups including solution type, analyze setup, and sweep algorithms in HFSS stay the same. Fig. 3.11 compares the return loss and insertion loss of the two structures, from which we can see that the results are almost the same. If we use $|S_{11}|$ (in linear scale frequency response) to define the error of such a device to be:

$$error = \frac{\sum_{i=1}^{P} \left| \frac{\left\|S_{11}\right\|_{fine} - \left\|S_{11}\right\|_{coarse}}{\left\|S_{11}\right\|_{fine\_\max} - \left\|S_{11}\right\|_{fine\_\min}} \right|}{P} \times 100\% \tag{3.6}$$

where the $P$ denotes the total number of solution frequency point. The calculated error is 6.24%, which successfully proves the consistence between the fine and the coarse model in a very wide frequency range. To get more information about the error of the coarse model, we need to go to Fig. 3.11. Generally, there are some insignificant phase shift in the passband of the device especially in the frequency range of 25-48GHz. The frequency shift caused the error of the coarse model. Despite there are some errors, Fig. 3.11 has told us that the coarse model has very close S-parameter response including $|S_{11}|$ and $|S_{21}|$.

Therefore, the surrogate coarse model can be validated at least for very basic SIW structures.

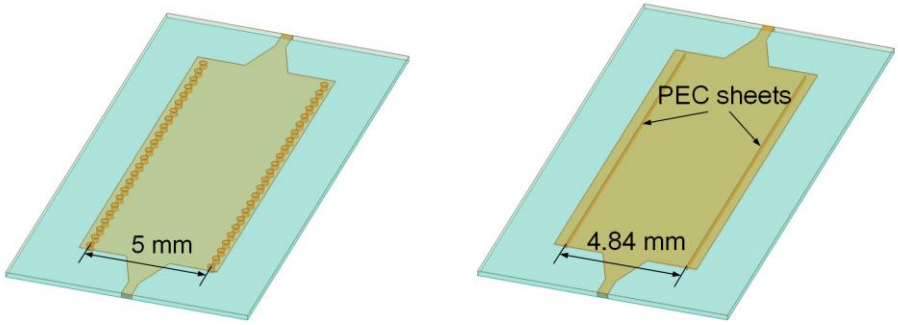


a. b.

Fig. 3. 10. The fine and coarse models of the SIW (a. fine model, b. coarse model).

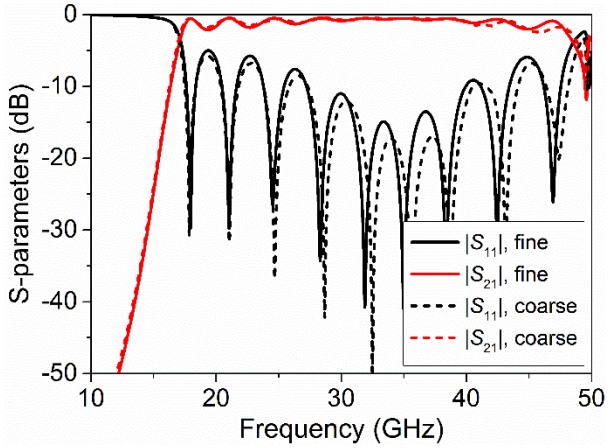


Fig. 3. 11. Return loss of the fine and coarse model of the SIW.

Next, let us consider a more complicated case: a published mm-wave antenna work using SIW technique [57]. Its configuration is shown in Fig. 3.12 and the values of parameters are given in Table. 3.2. The SIW cavity works as a power splitter to feed four dipoles such that the antenna achieved an omnidirectional radiation pattern. Because this configuration is obviously not a basic SIW structure, it cannot be directly optimized. According to (3.4) and (3.5), we can obtain the effective width and length of the SIW cavity, which are 3.22 mm and 14.33 mm, respectively. Next, a surrogate model was built as shown in Fig. 3.13.

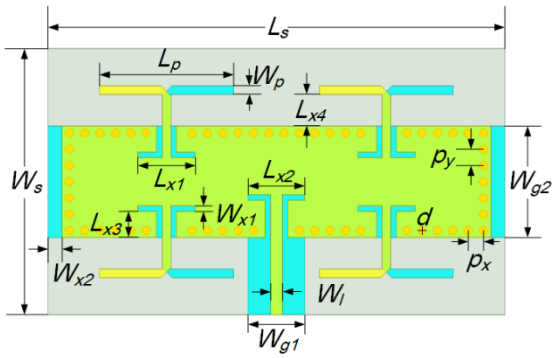


Fig. 3. 12. Configuration of the antenna [57].

Table 3. 2. Parameters of the antenna [57]

| Parameters | Value (mm) | Parameters | Value (mm) |
|---|---|---|---|
| $L_s$ | 16 | $W_s$ | 0.9125 |
| $L_p$ | 4.7 | $W_p$ | 0.3 |
| $L_{x1}$ | 2 | $L_{x2}$ | 2 |
| $L_{x3}$ | 0.9 | $L_{x4}$ | 1 |
| $W_{x1}$ | 0.2 | $W_{x2}$ | 0.5 |
| $W_l$ | 0.4 | $W_{g1}$ | 2 |
| $W_{g2}$ | 3.9 | $p_x$ | 0.54 |
| $p_y$ | 0.57 | $d$ | 0.3 |

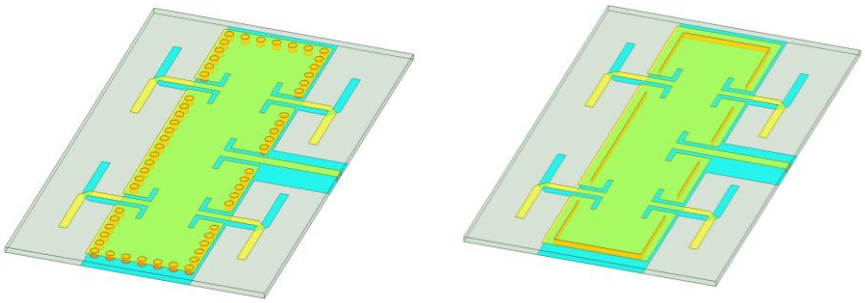

a. b.

Fig. 3. 13. The fine and coarse models of the antenna (a. fine model, b. coarse model).

Fig. 3.14 and Fig. 3.15 compare the simulation results of the two models, which show that the simulated return loss and the radiation patterns of the fine and coarse model match well. Although there is also some frequency shift, the error of the coarse model return loss is only 2.14%. On the other side, the simulated radiation patterns of the two models are almost identical. In fact, since the radiation parts, dipoles, have not been changed, such close radiation patterns are reasonable.

The results successfully validated the simplified approach for modeling SIW structures. With the surrogate coarse mode, one does not need to consider the via holes during optimization, that is, all the parameters related to the via holes do not need to be optimized. Therefore, the manual process described previously for optimizing parameters of via holes will be avoided. After optimization, the coarse model can be converted to the fine SIW model directly. Such an approach will remarkably improve the optimization efficiency of an SIW structure.

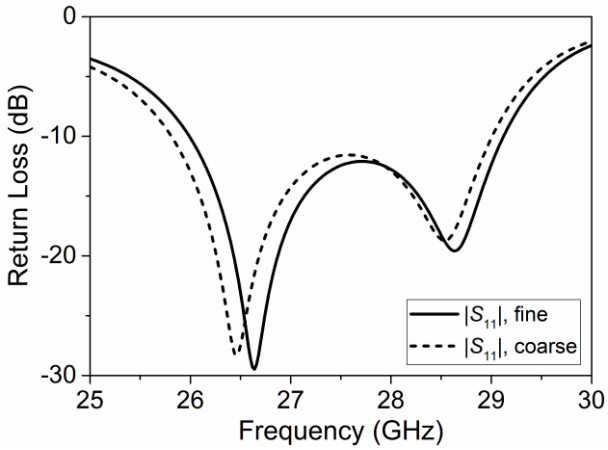


Fig. 3. 14. Return loss of the fine and coarse model of the antenna.

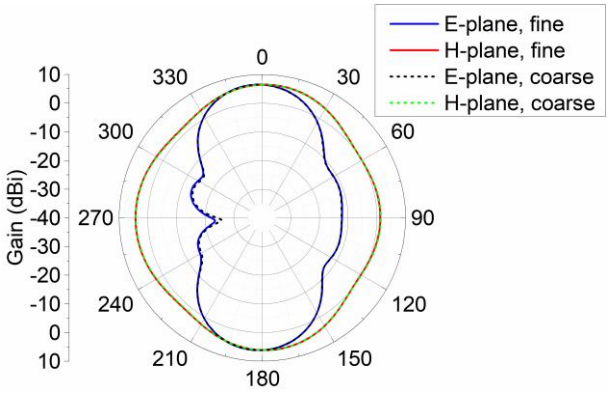


Fig. 3. 15. Radiation patterns of the fine and coarse model of the antenna.

## 3.4 Complete procedure of designing SIW devices

Based on previous research works done by other researchers and the SIW modeling approach proposed, we have a complete procedure of designing SIW devices such as antennas, power splitters, couplers, etc. Following this procedure strictly can design a device very quickly and accurately.

### 3.4.1 Calculating width and length

Since an SIW can be regarded as an RWG as aforementioned, the cut-off frequency of the dominant model can be calculated by either [58]

$$f_c = \frac{c}{2\sqrt{\varepsilon_r}}\sqrt{\left(\frac{1}{L_{eff}}\right)^2 + \left(\frac{1}{W_{eff}}\right)^2} \tag{3.7}$$

or [30]

$$f_c = \frac{c}{2\sqrt{\varepsilon_r}}\sqrt{\left(\frac{1}{W_{eff}}\right)^2} \tag{3.8}$$

where $c$ is the speed of light in free space and $\varepsilon_r$ is the relative permittivity of the substrate. Recall that $W_{eff}$ and $L_{eff}$ are the effective width and length of the SIW, respectively. (3.7) is for general cases, for example, an SIW cavity as the one adopted like Fig. 3.13, whose length is in the order of its width. While (3.8) is for the case that the length of the SIW is considerably larger than its width such that the term $(1/L_{eff})^2$ can be ignored.

In the proposed modeling approach, we do not need to consider the physical width and length of the SIW until we finish the optimization process and go to fabrication. Based on the targeted operating frequency bands and a given substrate (with a known $\varepsilon_r$), we can at first calculate the $W_{eff}$ and $L_{eff}$ by (3.7) or (3.9). For (3.7), an equation with two unknowns cannot be solved directly, but we are not doing some very accurate calculations, which is in fact not necessary. One can set an extra condition, e.g., $W_{eff} = L_{eff}$, which should be based on the configuration of the device to be designed. For (3.8), things are easier, one can directly solve

$$W_{eff} = c/2f_0\sqrt{\varepsilon_r} \tag{3.9}$$

to get the effective width of the SIW, or in other words, the physical width of the surrogate model we will use in simulation and optimization. The value length, on the other side, should be decided on the specific device and application.

### 3.4.2 Microstrip-to-SIW transition

Several types of feeding techniques for SIW including probe feeding, microstrip line feeding, and coplanar feeding have been studied and proposed in recent years [59]-[61]. Here we considered using microstrip lines to feed SIWs since this type of feed topology is simple and can be easily optimized. To match the SIW device with the feed line, usually with 50 Ω of characteristic impedance, a transition is necessary.

The tapered transition (Fig 3.9) has been largely adopted because of its simple structure, very low losses, capability to cover the whole bandwidth of the SIW as well as its better performance compared to other microstrip-to-SIW transitions or coplanar transitions [61]. Therefore, in this research, the tapered transition was implemented.

In D. Deslandes's works, an empirical equation for calculating the width of tapered microstrip-to-SIW transition has been obtained by EM simulations [61]. The equation is

$$\frac{4.38}{W_{eff}}\exp\left(-0.627\frac{\varepsilon_r}{\frac{\varepsilon_r+1}{2}+\frac{\varepsilon_r-1}{2\sqrt{1+12h/W_t}}}\right)=\begin{cases}\dfrac{60}{\sqrt{\frac{\mu_0}{\varepsilon_0}}h}\ln\left(8\dfrac{h}{W_t}+0.25\dfrac{W_t}{h}\right) & \text{for } \dfrac{W_t}{h}<1\\ \dfrac{120\pi}{\sqrt{\frac{\mu_0}{\varepsilon_0}}h\left[\frac{W_t}{h}+1.393+0.667\ln\left(\frac{W_t}{h}+1.444\right)\right]} & \text{for } \dfrac{W_t}{h}\geq 1\end{cases} \tag{3.10}$$

where $\mu_0$ and $\varepsilon_0$ are the permeability and permittivity of free space, respectively, and $h$ is the thickness of the substrate. For a given substrate ($h$ and $\varepsilon_r$ are known) and SIW or surrogate model ($W_{eff}$ is known), solving the above equation allows obtaining an optimum taper width $W_t$. On the other hand, the optimum taper length $L_t$ should be a multiple of a quarter guide wavelength to minimize the return loss [61].

### 3.4.3 Guide wavelength

Since SIW has similar behavior with RWG, its guide wavelength $\lambda_g$ for the dominant mode can be expressed as [49]:

$$\lambda_g=2\pi\Big/\sqrt{\frac{\varepsilon_r\left(2\pi f\right)^2}{c^2}-\left(\frac{\pi}{W_{eff}}\right)^2} \tag{3.11}$$

where $f$ is the operating frequency of the SIW.

### 3.4.4 Design procedure

According to the above discussions, to design an SIW device with tapered microstrip-to-SIW transition, we can follow the suggested steps:

1. For a specified operating frequency and substrate, use (3.9) or (3.11) to calculate the surrogate physical width $W_{eff}$ and length $L_{eff}$ (we will set a value based on the specific applications if we use (3.11)).

2. Calculate the width of the tapered microstrip-to-SIW transition using (3.10), and its length.

3. Build a surrogate model, that is, use PEC sheets to replace the periodic via holes.

4. Run an optimization round if deemed necessary.

5. Determine $d$ and $p$ based on the rules (3.2) and (3.3), calculate the SIW physical width $W_s$ and length $L_s$ using (3.4) and (3.5), respectively. Build a fine model of the device, and simulate it for verification, normally no extra optimization processes are needed.

## 3.5 Error analysis

Although the error of such an approach has been proved to be small such that the coarse model can be converted to fine model directly without any post-process, it is worth to know how the coarse model can be as accurate as possible.

Let us still use the antenna shown in Fig. 3.12 to analyze the error. Assume we used the coarse model (Fig. 3.13.b) to complete the optimization process and wish to convert it to fine model for the last round of simulation and fabrication. The physical width and length of the coarse SIW model are 3.22 mm and 14.33 mm, respectively. The final coarse model simulation results are shown in Fig. 3.16 (black solid lines). Now, we need to determine the values of $d$ and $p$, and the physical width $W_s$ and length $L_s$ of SIW, to build a fine SIW model. Note that this is a procedure (which just have been presented) we need to follow if we use such an approach to design a SIW device.

Recall that we have two rules for $d$ and $p$, (3.2) and (3.3), and since determined, $W_s$ and $L_s$ can be obtained from (3.4) and (3.5). We set four groups to evaluate how $d$ and $p$ affect the error, each group having three sets of values. Table 3.3 lists the four groups of $d$ and $p$ and their corresponding $W_s$, $L_s$, center frequency $f_0$, and error. Each of these physical parameter values was adopted to build a fine model while the other parameters are kept fixed. As discussed previously, the coarse models of both the basic SIW structure and the antenna had some frequency shift phenomenon in terms of S-parameters. Therefore, the enter frequency of each coarse model is presented in the table for comparison purpose. Note the center frequency of the coarse model is 27.410 GHz.

Fig. 3.16 presents the simulated $|S_{11}|$ of these fine models as well as that of the coarse model. Note that we have another constraint, i.e., the SIW structure should inherently satisfy (3.1) because the number of via holes has to be an integer. For example, the $p$ of $G_{1\text{-}1}$ is 0.4 mm, and $L_s$ = 14.57 mm; following (3.1) we have the number of via holes along one direction $N$ = 37.425. This is obviously unreasonable and unrealistic. Therefore, we did a post-process to adjust the calculated value of $N$, then recalculated $p$ following (3.1) to get a value very close to that we calculated from theoretical equations. Here, we manually determined $N$ to be 37, such that $p$ = 0.4047 mm. It is worth to emphasize that we just tried to investigate how the error relates to the $d$ and $p$ determined and how it can be decreased as much as possible. In this case, the post-process will not cause losing of generality or getting a wrong conclusion. Such a post-process will assure that the SIW structure can be modeled and fabricated physically.

Table 3. 3. List of parameters and their error

| Groups | $d$ | $p$ | $W_s$ | $L_s$ | $f_0$ | Error |
|---|---|---|---|---|---|---|
| $G_{1-1}$ | 0.3 mm | 0.4 mm | 3.46 mm | 14.57 mm | 27.375 GHz | 5.22 % |
| $G_{1-2}$ | 0.3 mm | 0.5 mm | 3.41 mm | 14.52 mm | 27.535 GHz | 3.40 % |
| $G_{1-3}$ | 0.3 mm | 0.6 mm | 3.38 mm | 14.49 mm | 27.600 GHz | 5.45 % |
| $G_{2-1}$ | 0.5 mm | 0.6 mm | 3.66 mm | 14.77 mm | 26.870 GHz | 20.78 % |
| $G_{2-2}$ | 0.5 mm | 0.8 mm | 3.55 mm | 14.66 mm | 27.200 GHz | 16.81 % |
| $G_{2-2}$ | 0.5 mm | 1.0 mm | 3.48 mm | 14.59 mm | 27.005 GHz | 12.91 % |
| $G_{3-1}$ | 0.3 mm | 0.6 mm | 3.38 mm | 14.49 mm | 27.600 GHz | 5.45 % |
| $G_{3-2}$ | 0.4 mm | 0.6 mm | 3.50 mm | 14.61 mm | 27.340 GHz | 9.61% |
| $G_{3-3}$ | 0.5 mm | 0.6 mm | 3.66 mm | 14.77 mm | 26.870 GHz | 20.78% |
| $G_{4-1}$ | 0.4 mm | 0.8 mm | 3.43 mm | 14.54 mm | 27.445 GHz | 5.60% |
| $G_{4-2}$ | 0.5 mm | 0.8 mm | 3.55 mm | 14.66 mm | 27.200 GHz | 16.81% |
| $G_{4-3}$ | 0.6 mm | 0.8 mm | 3.69 mm | 14.80 mm | 26.865 GHz | 22.86% |

The selected values have covered a very large range. A worst-case error of 22.86% while the smallest is only 5.22% (the final fine model adopted reaches to 2.14%). To achieve a small error, the diameter of the via holes should not be too large according to the presented results, e.g., the errors of group 2 is obviously larger than those of group 1. Also, the error of group 3 and group 4 also demonstrated that the consistence between fine and coarse model will be sacrificed with larger via holes.

The conclusion may need more data or theoretical analysis to be proved. However, with more data, more constraints can be set to make sure the error is small enough and has no impact on direct conversion from coarse model to fine model for fabrication. All of the selected values strictly followed the rules (3.2) and (3.3), but these rules are for building a correct SIW structure to avoid power leakage problem. Therefore, some groups showed large errors, and more rules for determining *d* and *p* are needed. However, without more strict rules, some large error can also be avoided by straightforwardly adopting more “reasonable” configuration.

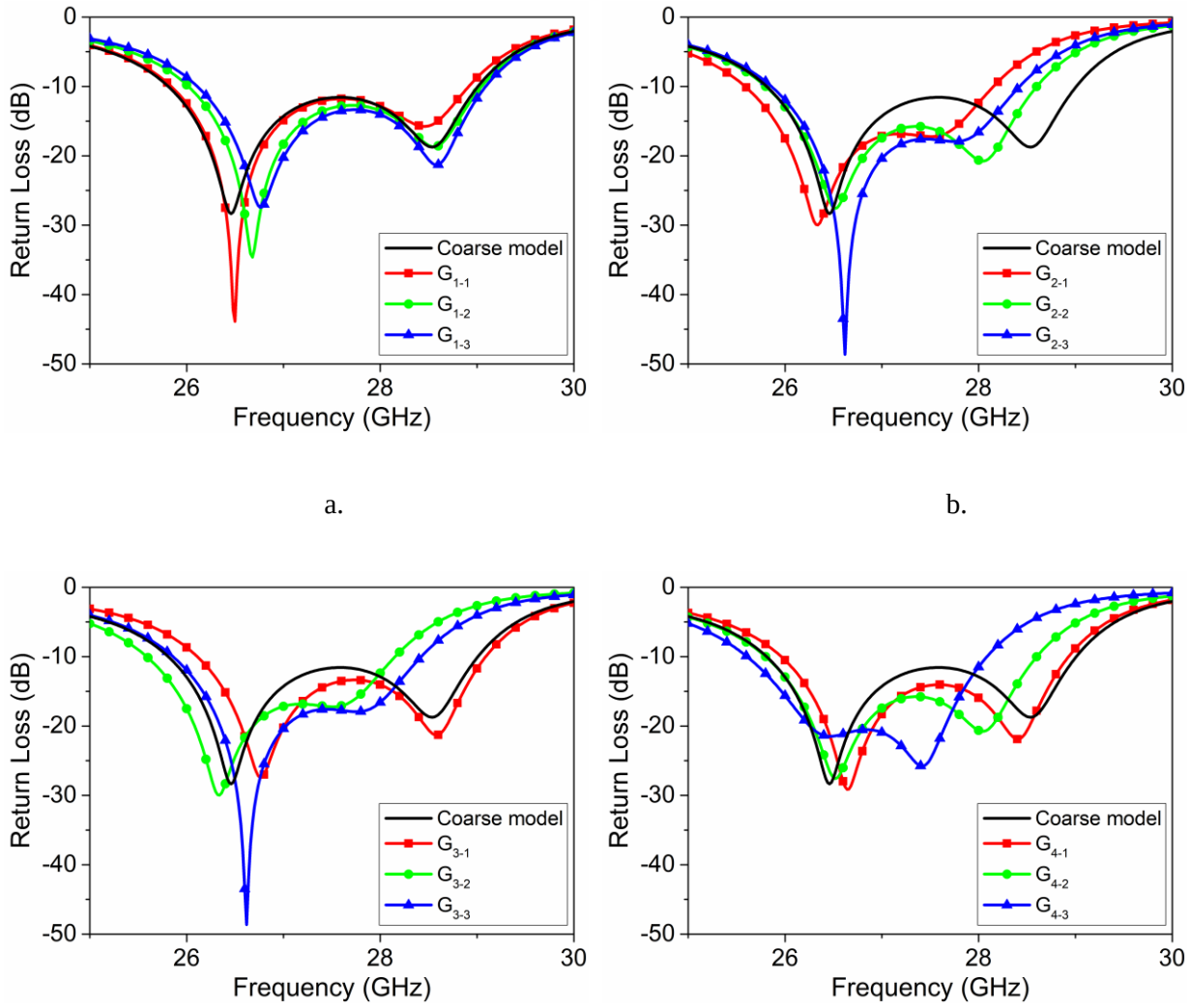


Fig. 3. 16. Return loss of the antenna with different values of *p* and *d* (a. group 1, *d* = 0.3 mm, while *p* equals to 0.4 mm, 0.5 mm, 0.6 mm, respectively, b. group 2, *d* = 0.5 mm, while *p* equals to 0.6 mm, 0.8 mm, 1.0 mm, respectively, c. group 3, *p* = 0.6 mm, while *d* equals to 0.3 mm, 0.4 mm, 0.5 mm, respectively, and d. group 4, *p* = 0.8 mm, while *d* equals to 0.4 mm, 0.5 mm, 0.6 mm, respectively).

Fig. 3.17 compares the configuration of the antenna of $G_{4\text{-}1}$ and $G_{4\text{-}3}$, from which we can see that the via holes of $G_{4\text{-}3}$ is relatively large compared to the antenna. Despite the error of $G_{4\text{-}1}$ is smaller than that of $G_{4\text{-}3}$ (since we do not know the errors when determining the values of *d* and *p*), one would select $G_{4\text{-}1}$ just because the via holes of $G_{4\text{-}3}$ are really large and looks abnormal. Therefore, we actually not only need to follow the rules (3.2) and (3.3) to determine *d* and *p* but have to consider the final configuration of the device to make it looks "reasonable".

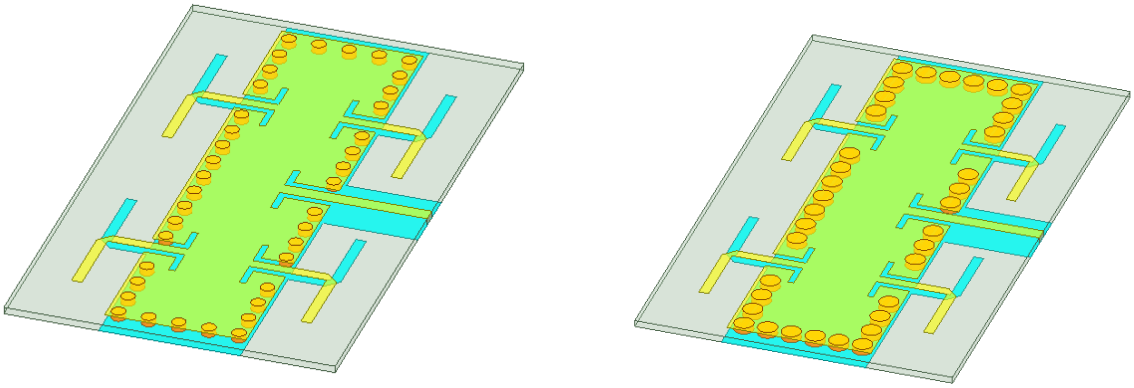

a. b.

Fig. 3. 17. Configurations of $G_{4\text{-}1}$ and $G_{4\text{-}3}$ (a. $G_{4\text{-}1}$, looks normal and b. $G_{4\text{-}3}$, the via holes are too large).

## 3.6 Conclusion

In this chapter, the difficulties and challenges of modeling SIW devices in 3D EM commercial software were discussed at first. Secondly, the work mechanism of RWGs and SIWs was introduced. Then, a new approach for SIW device simulations was proposed. The idea of the approach is replacing the SIW structure to be optimized by a surrogate coarse model. A basic SIW and a published antenna [57] were used for comparison and error analyzes, which proved that the proposed approach is accurate. Besides, a complete procedure of designing SIW devices was concluded. Following the procedure strictly, one can easily get initial values of the SIW device to be designed, and the optimization process will be timesaving with the proposed surrogated model of SIW.

# Chapter 4. Printed Quadrupole Antenna

In this chapter, a novel printed quadrupole antenna configuration is proposed. It consists of two symmetric dipoles and a ground placed such that the antenna can radiate power omnidirectionally without being influenced by the ground. More interestingly, such a configuration allows the feed network being integrated inside the elements without increasing the overall size of the array. Furthermore, no extra ground will be added, and omnidirectional radiation pattern will be maintained.

## 4.1 Conventional Printed Dipole Antenna

Dipole antennas offer a large panel of attractive features. They are inexpensive, very versatile, and can be found in numerous commercial products such as cellular phones, car radios, walkie-talkies, etc.

The radiation characteristics of dipoles have been widely analyzed and discussed. The proposed quadrupole antenna starts with a simple printed dipole antenna as shown in Fig. 4.1. Since the ground works as a reflector, the antenna cannot achieve an omnidirectional radiation pattern as demonstrated in Fig. 4.2. This type of so-called quasi-omnidirectional antenna has been utilized for 5G handset devices [17]. It is also usually used as driven element to design Yagi-Uda antennas and arrays that can provide more focused beams [62]-[65].

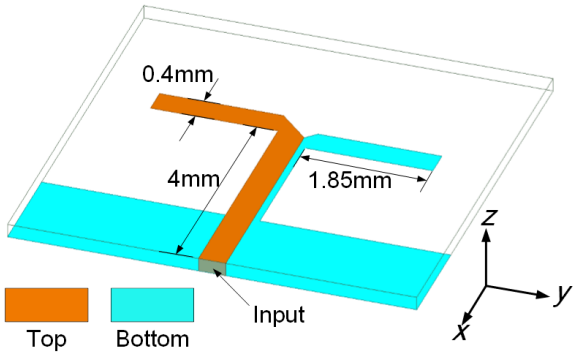


Fig. 4. 1. Configuration of the printed dipole antenna operating at 26GHz.

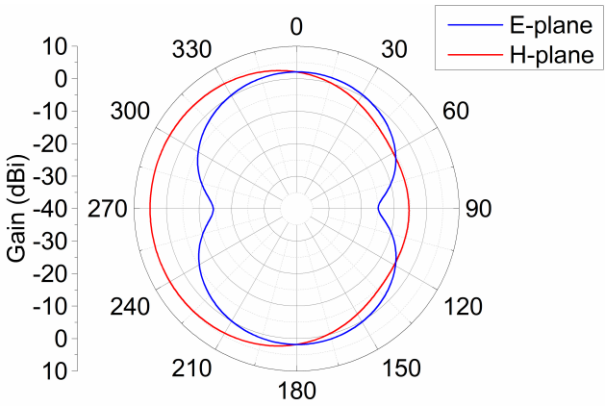


Fig. 4. 2. Simulated radiation pattern of the printed dipole antenna.

One can, of course, adjust the size of the ground to achieve a more omnidirectional pattern, but the input impedance of the antenna will be affected. Some other options have been also investigated, but they mainly lead to a complex configuration, such as those described in [12], [15], and [16]. Alternatively, one can add the same dipole at the opposite direction as shown in Fig. 4.3. The planar omnidirectional antennas described in [7] and [57] are based on similar configuration and both achieved relative high gain with small size.

## 4.2 Omnidirectional Printed Quadrupole Antenna

The proposed printed quadrupole antenna [66] is shown in Fig. 4.3. Fed by a microstrip power splitter, the antenna is symmetric around the *y*-axis. Fig. 4.4 shows the simulated radiation patterns of such a quadrupole antenna, highlighting an omnidirectional radiation pattern at the H-plane. Fig. 4.5 straightforwardly compares the radiation characteristics of the dipole and the quadrupole; since another radiation part is added, the quadrupole antenna can radiate power omnidirectionally as indicated in Fig. 4.5.b. In contrast, the conventional dipole can only radiate power directionally.

Meanwhile, the quadrupole antenna still keeps the attractive features of the conventional printed dipole antennas. It exhibits good performance in terms of both bandwidth and gain, i.e., a -10 dB impedance bandwidth of 3.3 GHz and an enhanced gain of 5.5 dBi (Fig. 4.6). Furthermore, it also has a broad pattern bandwidth (Fig. 4.7). From the fabrication point of view, this low-profile antenna is cost-efficient because of its simple 2D structure and fabrication process.

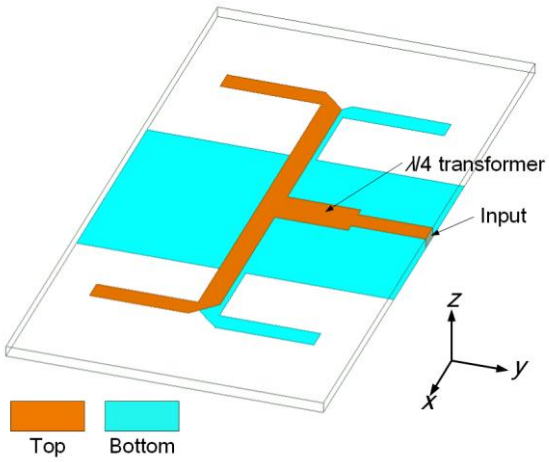


Fig. 4. 3. Configuration of the printed quadrupole antenna.

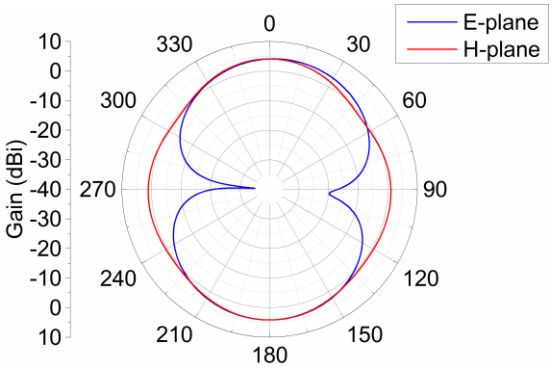


Fig. 4. 4. Simulated radiation pattern of the printed quadrupole antenna.

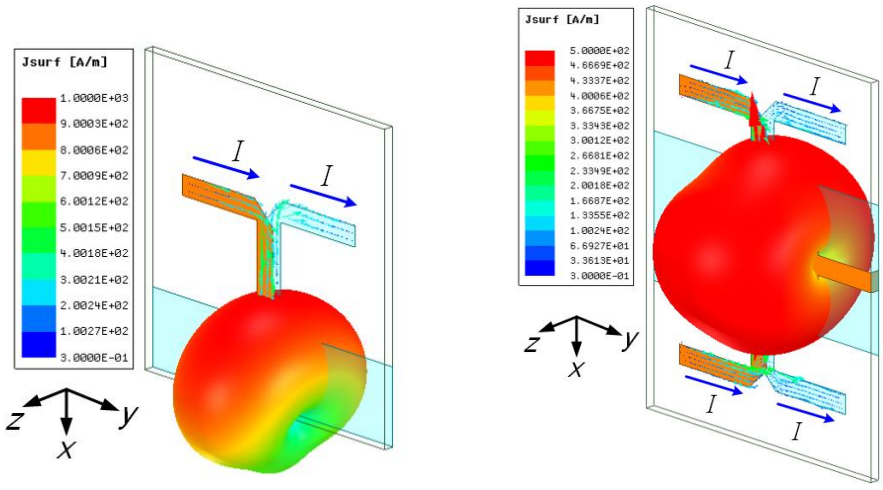


a. b.

Fig. 4. 5. Simulated 3D radiation patterns and surface current distributions of the two antennas (a. conventional dipole, b. quadrupole).

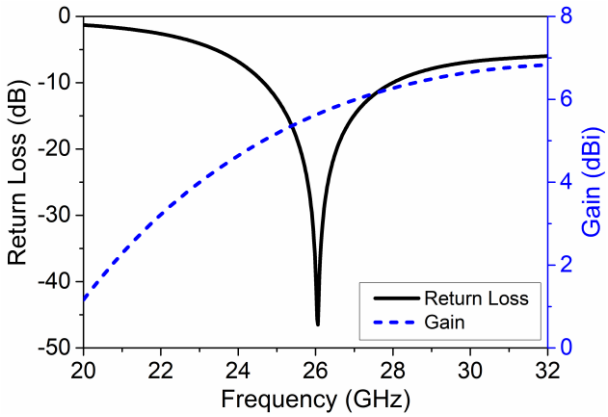


Fig. 4. 6. Simulated return loss and gain of the quadrupole antenna.

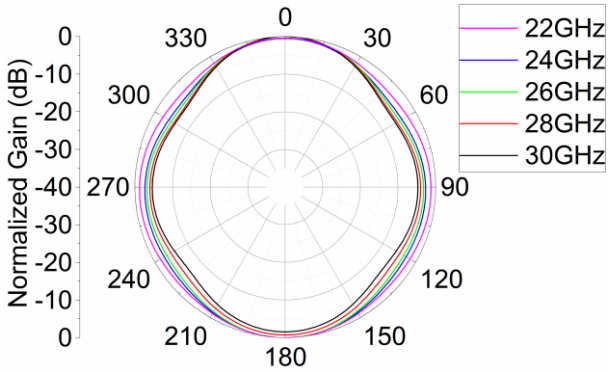


Fig. 4. 7. Simulated radiation patterns at H-plane of the quadrupole antenna at various frequencies.

## 4.3 Printed Quadrupole Antenna Array

As mentioned above, in the mm-wave band, high gain antennas are always preferred. Even though the quadrupole antenna has many attractive features, its gain (5.5 dBi) is not enough for 26 GHz applications. In this case, we need to build an array.

### 4.3.1 An ideal 1 × 8 array

To get an omnidirectional radiation pattern, the antenna elements should be arranged along the current flow direction, i.e., *y*-axis, as shown in Fig. 4.8 for a 1 × 8 array (with a uniform space of 7 mm).

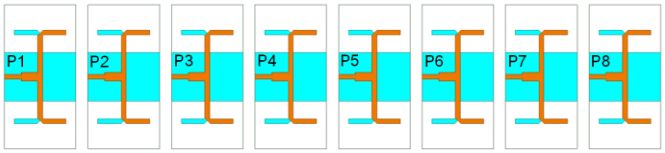


Fig. 4. 8. Linear array (without feed network) consists of eight quadrupole antennas.

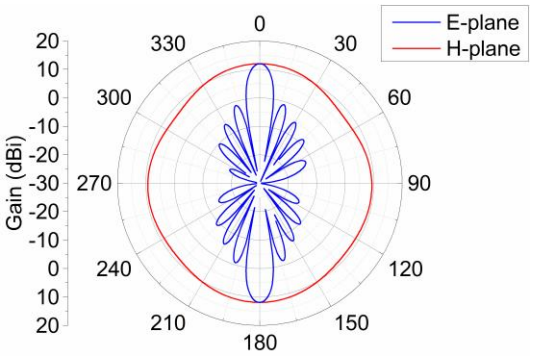


Fig. 4. 9. Simulated Radiation pattern of the linear array (without feed network).

When a uniform power distribution is applied, the array presents a high gain with an omnidirectional pattern, as shown in Fig. 4.9. However, this is an ideal case; the simulations did not include the feed network, which is essential.

### 4.3.2 Existing feed networks and their constraints

Because of the arrangement of the elements, it is not easy to adopt conventional series or parallel feed network (Fig. 4.10) here. One can add microstrip lines perpendicular to the feed lines of the elements, and then implement a conventional microstrip line feed network, as shown in Fig. 4.11. However, beside the considerable losses of microstrip lines, there are still two major problems that need to be addressed at such high frequencies: (i) microstrip lines can generate undesired radiations that might deform the radiation pattern of the array and (ii) a very large ground plane should be added, which will work as a reflector that will degrade the omnidirectional radiation pattern.

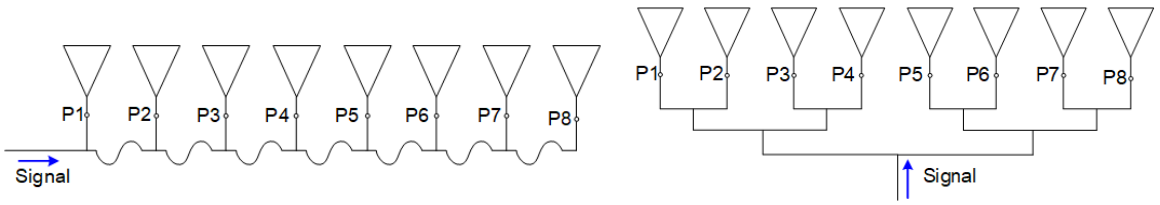


a. b.

Fig. 4. 10. Conventional feed networks for antenna arrays (a. series feed, b. parallel feed.) Since the input ports of the array shown in Fig. 4.8 are located “inside” the device, neither of these feed techniques can be directly applicable to the array.

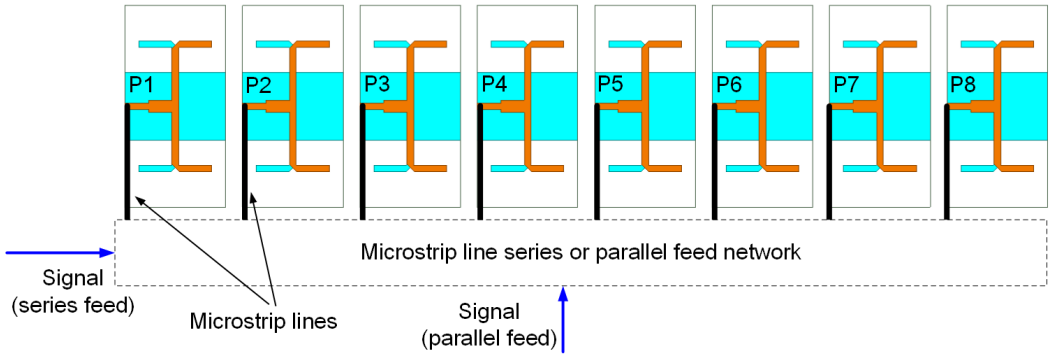


Fig. 4. 11. A way to implement conventional microstrip line feed networks. However, this is not feasible mainly because the ground of the microstrip lines will degrade the omnidirectional radiation pattern.

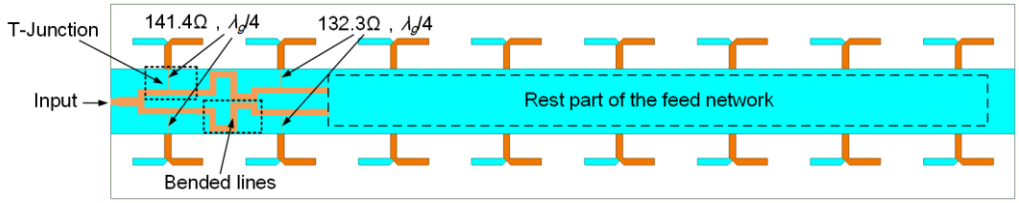


Fig. 4. 12. A Possibly feasible way to implement microstrip line feed network. However, some lines will be extremely narrow, and some lines might overlap.

Instead of implementing conventional feed networks, new ways should be explored, like the configuration shown in Fig. 4.12.

When the distance between too symmetric dipoles is fixed (the impact of this parameter on the directivity of the antenna will be discussed in Chapter 6), there will be at least three issues to tackle:

1. T-junctions will consist of some very narrow microstrip lines. For example, even in the uniform power distribution case, there is a microstrip line with characteristic impedance of 141.4 Ω (0.013mm on this substrate) in the first T-junction, which is too narrow to be fabricated.

2. The feed network will be too tight. Such a limited space must include T-junctions and perhaps some bended lines for achieving desired phase progression.

3. Strong mutual coupling between lines might significantly degrade the array performance.

From the above constraints, the first one is particularly challenging, making the proposed feed network not practical.

However, as long as the dipoles can be fed properly, the array will exhibit many superior features as early discussed. So, the problem is finding an appropriate way to feed such a quadrupole array.

## 4.4 Conclusion

A new antenna configuration, namely printed quadrupole was proposed in this chapter. Printed quadrupoles are, in fact, a variant of printed dipoles. Compared to conventional printed dipoles, however, the proposed quadrupole has an enhanced gain and an omnidirectional radiation pattern. More importantly, the quadrupoles potentially allow feed network to be integrated inside of them to build omnidirectional antenna arrays.

However, as discussed in this chapter, it is difficult to exploit existing widely used feed networks to feed the designed quadrupole. In this case, it is almost not possible to feed a quadrupole antenna with eight or more elements array using conventional microstrip feeding topology. In this, we need to explore a new feeding topology.

A new way of feeding, which can feed quadrupoles to build an omnidirectional array, will be proposed in the next chapter. Such a topology is based on the well-known SIW technique.

# Chapter 5. LSIW Feed Network

In this chapter, we present a novel feed network using a long SIW (LSIW) to feed the quadrupole antenna array proposed in Chapter 4. As its name indicates, the length of the SIW will be considerably larger than its width. Besides, the proposed feed network will have a broad impedance bandwidth and can provide output power with equal magnitude and phase at all the output ports.

## 5.1 Configuration

Fig. 5.1 shows the configuration of the proposed novel feed network. The designed novel LSIW feed network has one input port and 16 output ports to feed eight quadrupole antennas. The optimized parameters of the feed network are given in Table 5.1. It is worth to mention that the optimization target is to get good return loss as well as uniform output power (with equal amplitude and phase) at 26 GHz. Note that in order to significantly lighten the optimization round, the variation range and the step-size of the parameters to optimize were predefined.

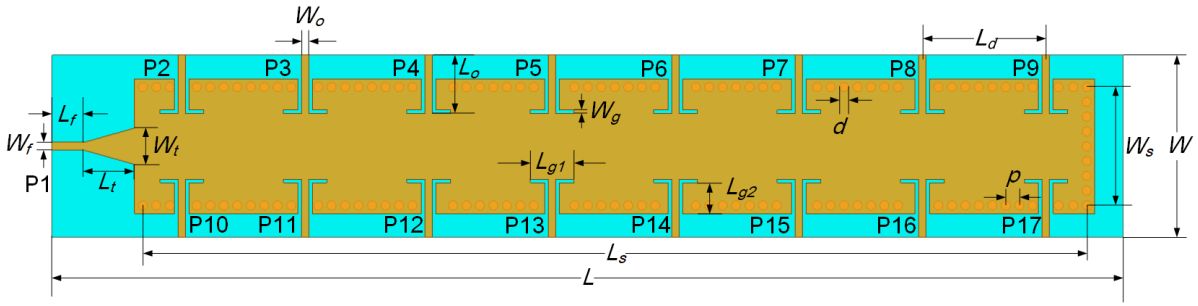


Fig. 5. 1. Configuration of the proposed novel feed network.

Table. 5. 1. Optimized parameters of the novel feed network

| Parameters | Value (mm) | Parameters | Value (mm) |
|---|---|---|---|
| $W_f$ | 0.426 | $L_{g2}$ | 1.7 |
| $L_f$ | 1.75 | $d$ | 0.5 |
| $W_t$ | 2 | $p$ | 0.75 |
| $L_t$ | 2.8 | $L_d$ | 6.8 |
| $W_o$ | 0.4 | $W_s$ | 6.5 |
| $L_o$ | 3.2 | $L_s$ | 52 |

## 5.2 Simulated results

Since the feed network is symmetric, the S-parameters of only ports 1 to 9 are displayed (Fig. 5.2 and Fig. 5.3). Also, because all the output ports including slotlines are identical, Fig. 5.2 illustrates that this configuration inherently provides uniform output power distribution at one of its resonant frequencies, i.e., 26 GHz. Besides, compared to some existing power dividers [67]-[69], the insertion loss (12.95 dB) of the feed network is relatively low. Furthermore, the distance between two adjacent output ports $L_d$ is equal to the guide wavelength $\lambda_g$, such that all the output power is equiphase as shown in Fig. 5.3.

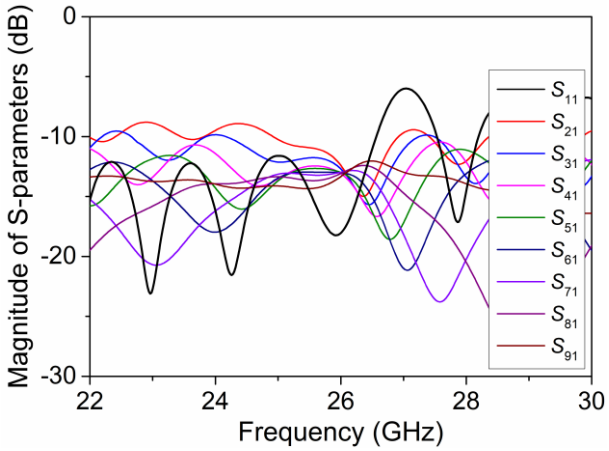


Fig. 5. 2. Simulated magnitude of S-parameters of the proposed novel feed network.

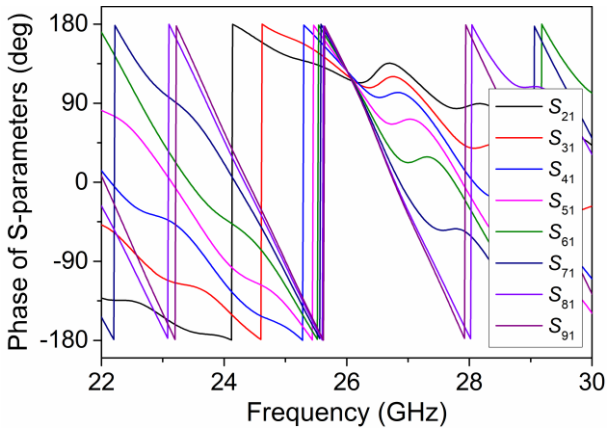


Fig. 5. 3. Simulated phase of S-parameters of the proposed novel feed network.

## 5.3 Design procedure

To design such a feed network, we can follow the steps suggested in the part 3.4.4 of Chapter 3. The targeted frequency is 26 GHz, and the substrate was chosen to be Rogers 4003C ($\varepsilon_r$ = 3.55, tan$\delta$ = 0.0027, $h$ = 0.203 mm). Since the length of the LSIW is much larger than its width, we at first follow (3.9) to calculate the physical width of the surrogate coarse model. Next, the guide wavelength $\lambda_g$ can be obtained by (3.11) to determine the distance between adjacent output ports $L_d$. Then, the width and length of tapered microstrip-to-SIW transition can be obtained by (3.10). Finally, a surrogate model as shown in Fig. 5.4 can be built.

Fig. 5.4 shows the optimized surrogate coarse model of the LSIW feed network. The width and length of the RWG (the coarse model of SIW) are 6.15mm and 51.65 mm, respectively, while the other parameters are kept the same as in the fine model shown in Fig 5.1. After optimization, when all simulated responses will satisfy the specifications, a fine model needs to be built for latter steps. Fig 5.5 shows the simulated results of surrogate coarse model of the LSIW feed network. Note that Fig. 5.2 and Fig. 5.3 are nearly identical. To illustrate the error of the coarse model, Fig. 5.6 compares the return loss of the coarse and the fine model (since we have too many S-parameters, we took the return loss as example), which tells that the error is really small, as expected. The diameter of via holes $d$ and space of via holes $p$ should be determined based on the rules (3.2) and (3.3). Also, the physical SIW width $W_s$ and length $L_s$ should be calculated by (3.4) and (3.5), respectively. A fine model can be then built.

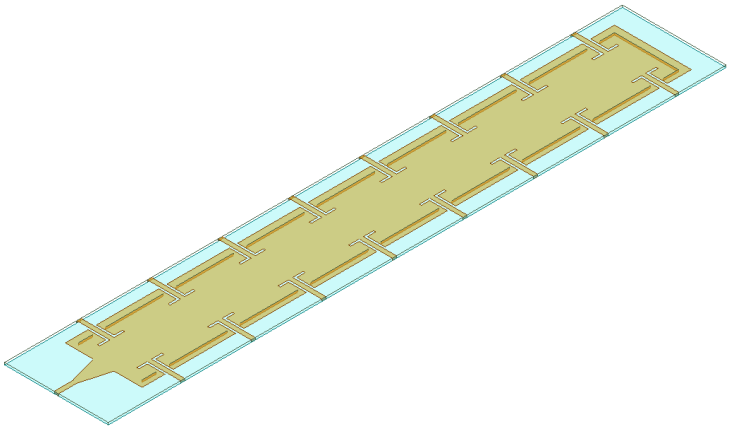

Fig. 5. 4. Surrogate coarse model of the LSIW feed network.

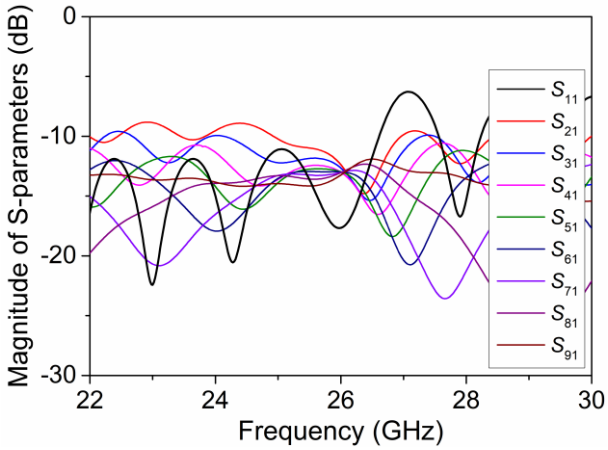


Fig. 5. 5. Simulated magnitude of S-parameters of the surrogate coarse model.

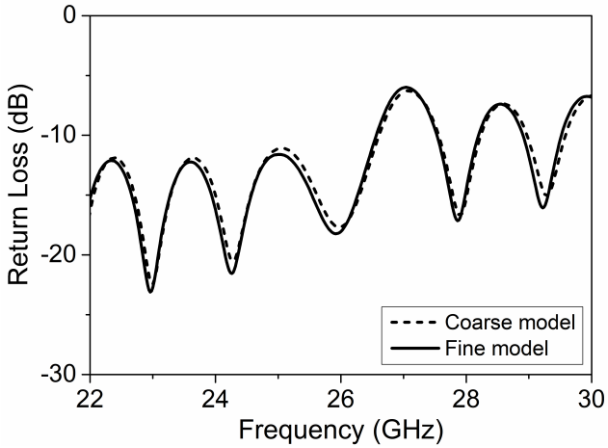


Fig. 5. 6. Simulated return loss of the fine and coarse model of the LSIW feed network.

Here the importance of the coarse model should be re-emphasized. Note that the two rows of metalized via holes actually have gaps on the positions of output ports. To get optimum results, all the parameters except the width and length of the 50Ω feed line need to be optimized. However, changing the value of some parameters will cause the deformation of the SIW structure such that the whole model would be invalid as previously discussed. For example, from the optimized model shown in Fig. 5.1, we found that the number of via holes between the first and the second output ports is eight (count from the left side to the right side). Let us call the first and the last one as "via 1" and "via 8", respectively. Assume we "duplicate" the very first via with a distance of $p$ $N$ times (with $N$ the total number of via holes) to get a row of via holes, which is a rather simply way of modeling SIW structures in HFSS, and we "delete" some of vias to model the gaps. In this example, we deleted the ones in front of via 1 and behind via 8 (Fig 5.7). We deleted specific vias based the calculated $L_d$, but this parameter usually needs to be optimized. If $L_d$ should

be larger to satisfy the requirements, we might need to be "re-delete" other vias and manually add previously deleted vias (Fig. 5.8). Also, notice that there are 16 gaps, that means a really complex process. So, we need to rebuild a model to run another round of simulation with a different value of $L_d$.

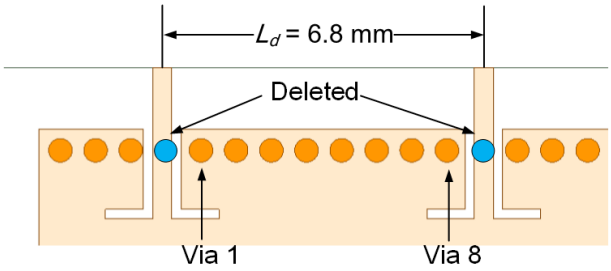


Fig. 5. 7. Zoomed in view of the LSIW feed network.

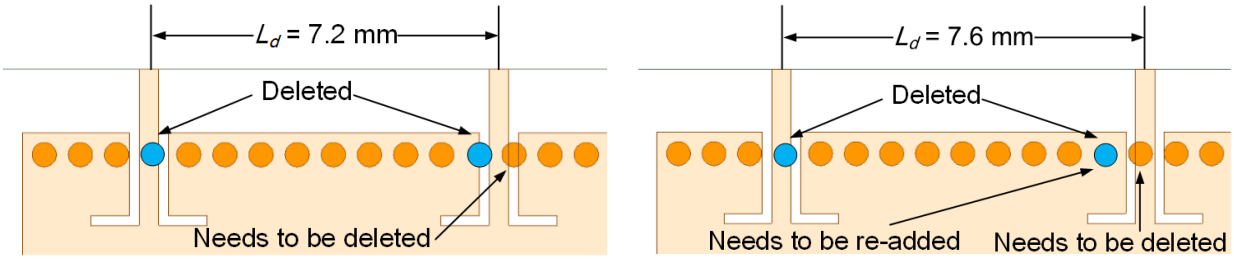


a. b.

Fig. 5. 8. Zoomed in view of the LSIW feed network with different $L_d$ while other parameters are fixed (a.

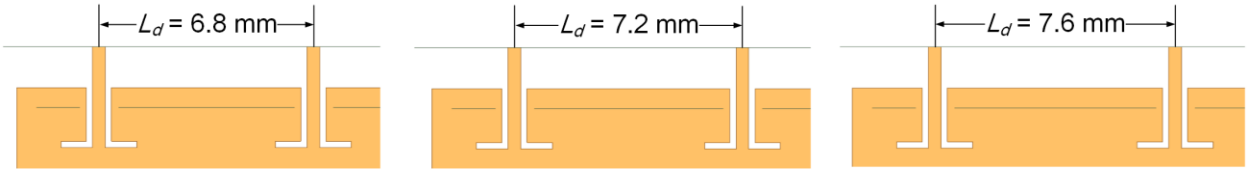


a. b. c.

Fig. 5. 9. Zoomed in view of the coarse model of the LSIW feed network with different $L_d$ while other parameters are fixed (a. $L_d$ = 6.8 mm, b. $L_d$ = 7.2 mm, and c. 7.6 mm).

Fortunately, with the coarse model, this will not be a problem since all the via holes are replaced by several pieces of PEC sheets. Optimizing the parameters will not cause deformation of the model. Fig. 5.9 shows a zoomed in view of the model with different values of $L_d$, the model is not deformed, and optimization process can be carried on easily and efficiently.

The simulated results of the coarse model verify the proposed surrogate model approach again; no extra optimization process is needed when the fine SIW model is built strictly based on the rules. This approach can be used for optimizing not only basic and simple SIW structures, but also rather complicated devices.

## 5.4 Key Design Parameters

According to (3.7) - (3.9), the LSIW width $W_s$ is the major factor determining the operating frequency of the device when $d$ and $p$ are properly fixed based on (3.2) and (3.3). To support this statement, Fig. 5.10 and Fig. 5.11 present the return loss of the feed network with various LSIW widths and lengths. In fact, Fig. 5.10 confirms that the operating frequency increases with the decrease of the LSIW width $W_s$ while Fig. 5.11 shows that the LSIW length $L_s$ has little impact on the return loss in the operating frequency band.

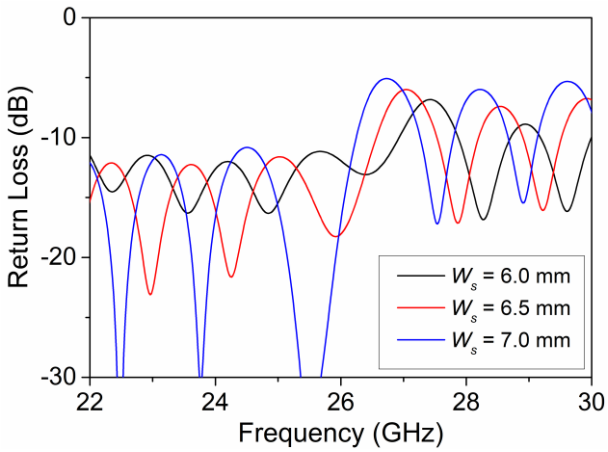


Fig. 5. 10. Simulated return loss of the proposed novel feed network with various LSIW width $W_s$ while other parameters are fixed.

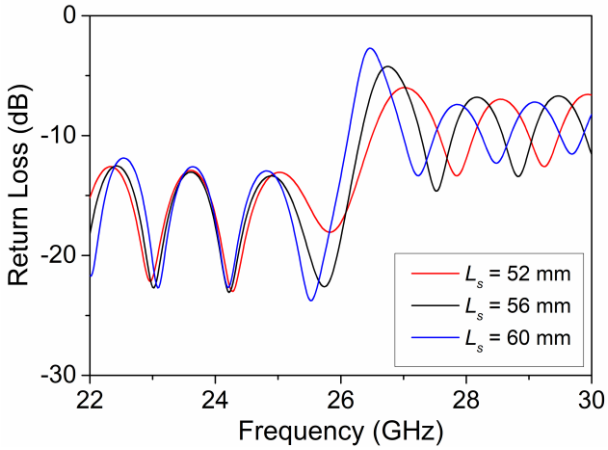


Fig. 5. 11. Simulated return loss of the proposed novel feed network with various LSIW length $L_s$ while other parameters are fixed.

Since $W_s$ is the main factor that influences the operating frequency, the simulated results shown in Fig. 5.2 could be improved like decreasing $W_s$ to reach the desired center frequency of 26 GHz. However, as previously discussed, decreasing $W_s$ will increase the guide wavelength $\lambda_g$, as stated by the surface current distribution shown in Fig. 5.12.

Hence, $L_d$ needs to be increased. However, changing $L_d$ could lead to mismatching of the device at our targeted frequency. More importantly, because this device will be used to feed antennas, $L_d$ determines the distance between too adjacent elements, which has a large impact on the shape of the radiation pattern of the array. Therefore, the biggest challenge of designing this device is finding the optimum value of the LSIW width. More importantly, every time $W_s$ changes, $L_d$ needs to be adjusted to maintain the phase progression of 0. Recalling how $L_d$ affects the via holes, using the surrogate model (Fig. 5.4) for optimization would be much efficient than directly using the fine SIW model (Fig. 5.1).

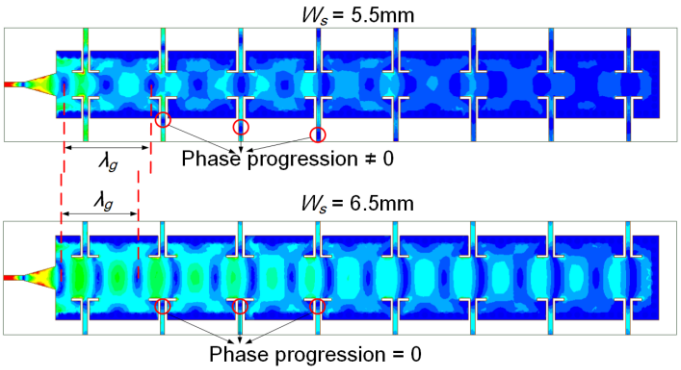


Fig. 5. 12. Simulated top surface current distribution of the proposed novel feed network at 26 GHz with different LSIW width $W_s$ while other parameters are fixed. The guide wavelength for $W_s$ = 5.5 mm being larger than that for $W_s$ = 6.5 mm, the phase progression in the above two cases is different.

In addition, the tapered transition is a key for impedance matching. So, its length $L_t$ and width $W_t$, without doubt, have impacts on the return loss of the proposed feed network. In fact, the slots at output parts can also affect the return loss. There are three parameters related to the slots, namely $W_g$, $L_{g1}$, and $L_{g2}$. Fig. 5.13 - 5.14 show the simulated return loss with various $W_g$, $L_{g1}$, and $L_{g2}$, respectively, which clearly indicate that these three parameters also need to be properly optimized.

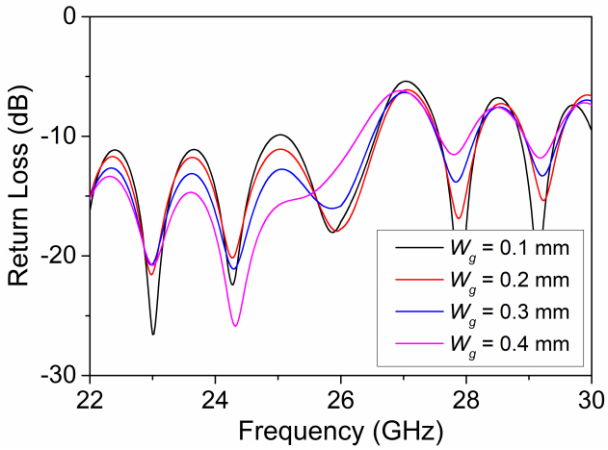


Fig. 5. 13. Simulated return loss of the proposed novel feed network with various $W_g$ while the other parameters are kept fixed ($L_{g1}$ = 2.4 mm and $L_{g2}$ = 1.7 mm).

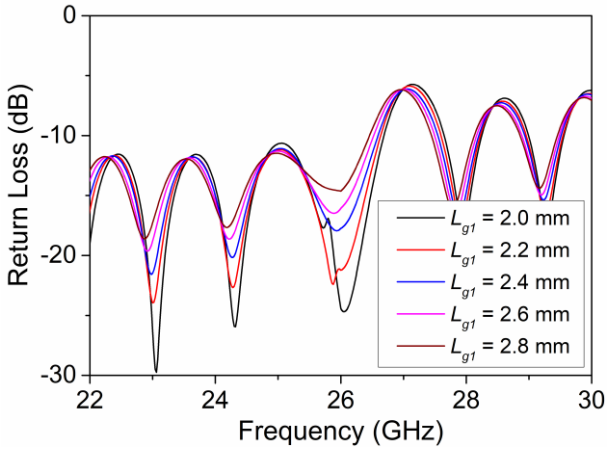


Fig. 5. 14. Simulated return loss of the proposed novel feed network with various $L_{g1}$ while the other parameters are kept fixed ($W_g$ = 0.2 mm and $L_{g2}$ = 1.7 mm).

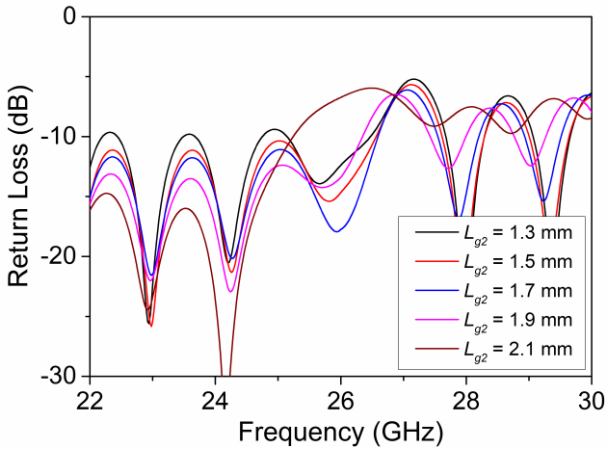


Fig. 5. 15. Simulated return loss of the proposed novel feed network with various $L_{g2}$ while the other parameters are kept fixed ($W_g$ = 0.2 mm and $L_{g1}$ = 2.4 mm).

## 5.5 Conclusion

A novel series fed network using SIW technique has been proposed in this chapter. Based on the well-known waveguide theory, this feed network was optimized to be able to provide uniform equiphase power to the antenna elements to be fed. Besides, its low loss feature was demonstrated by comparing with some existing SIW power dividers.

Its design procedure, including some necessary equations, was also discussed. One can follow the procedure to design an LSIW feed network easily.

# Chapter 6. Novel Printed Quadrupole Antenna Array

In this Chapter, a novel omnidirectional antenna array, fed by the LSIW feed network discussed in Chapter 5, is proposed.

## 6.1 Configuration

In this step, eight quadrupole antennas (described in Chapter 4) fed by the proposed feed network are combined in order to design an omnidirectional array. After optimization, the configuration and optimized parameters of the proposed antenna array are shown in Fig. 6.1 and given in Table 6.1, respectively. Fig. 6.2 shows the top surface current distribution, which indicates that the dipoles are fed in phase. The overall size of the array is 62 mm × 12 mm (5.37 $\lambda_0$ × 1.04 $\lambda_0$).

Fig. 6.3 shows the top and back view of the fabricated prototype of the proposed array. For the convenience of installing connector, the left side of the array is enlarged a little bit.

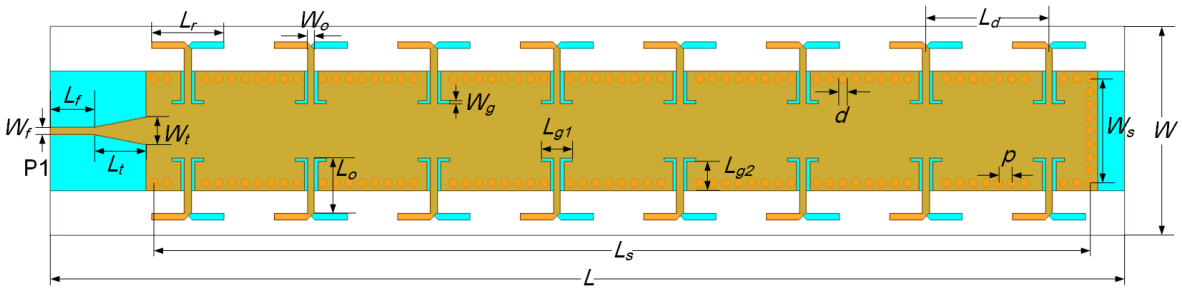


Fig. 6. 1. Configuration of the novel antenna array.

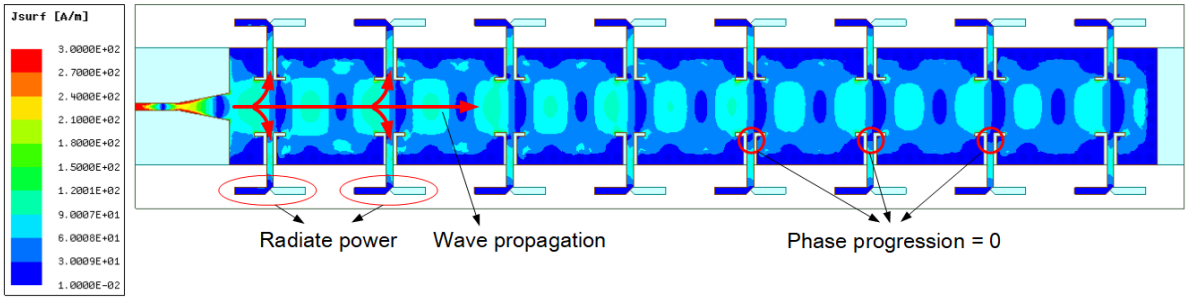


Fig. 6. 2. Simulated top surface current distribution of the proposed antenna array.

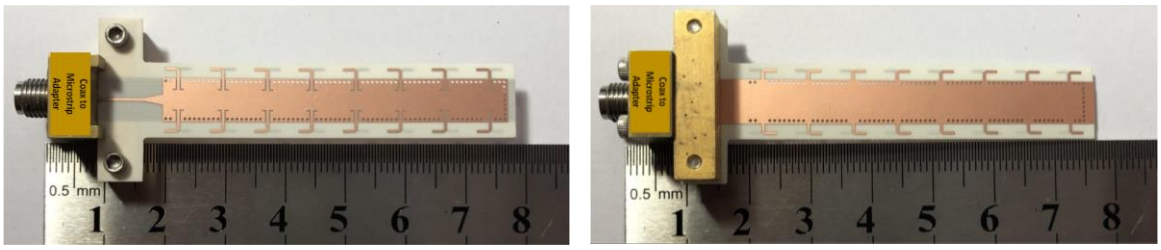


a. b.

Fig. 6. 3. Prototype of the proposed array (a. top view, b. back view).

Table. 6. 1. Optimized parameters of the novel antenna

| Parameters | Value (mm) | Parameters | Value (mm) |
|---|---|---|---|
| $W_f$ | 0.426 | $L_{g2}$ | 1.9 |
| $L_f$ | 2.55 | $d$ | 0.5 |
| $W_t$ | 1.6 | $p$ | 0.75 |
| $L_t$ | 3 | $L_d$ | 7.1 |
| $W_o$ | 0.4 | $W_s$ | 6 |
| $L_o$ | 3.2 | $L_s$ | 54 |
| $L_r$ | 4.2 | $W$ | 12 |
| $W_g$ | 0.2 | $L$ | 62 |
| $L_{g1}$ | 1.8 | | |

## 6.2 Surrogated model simulation

Same as for the feed network, a surrogate model (Fig. 6.4) was built for optimization process. The optimized dimension of the RWG is 5.65 mm × 53.65 mm while all other parameters are the same as in the fine model (Fig. 6.1). The simulation results of the surrogate coarse model are presented in the next section to compare them with the fine model simulation results.

Fig. 6.5 shows the optimized return loss, gain and efficiency of the array and Fig. 6.6 shows the normalized radiation patterns at 26GHz. These simulation results agree well with those of the fine model (which we will present in the next section) as expected.

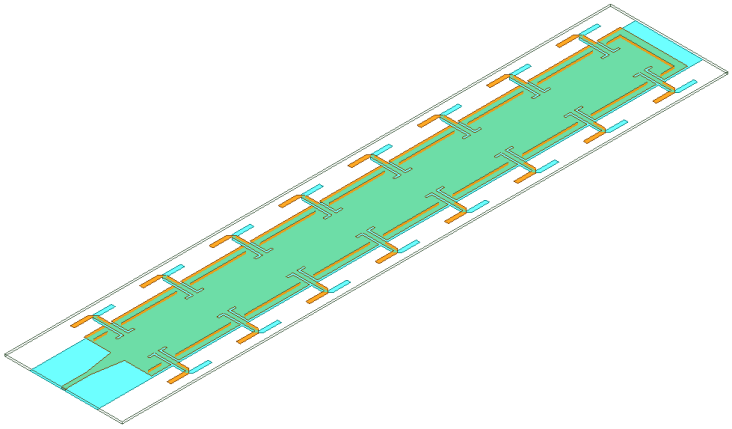

Fig. 6. 4. Surrogate coarse model of the proposed antenna array.

## 6.3 Performance

The coarse model was converted to fine model for the last round of simulation, and then fabrication and measurements. The converting process strictly followed the rules presented in Chapter 3, and no extra process has been done. The only part that is different is related to the PEC sheets, which were replaced by metalized vias.

### 6.3.1 Comparison of fine and coarse model simulation results

To further demonstrate the proposed coarse model approach in the design of the antenna array, we compared the simulated responses of the coarse model with the fine model.

Fig. 6.5 compares the return loss of the fine and the coarse model while Fig. 6.6 compares their gain and efficiency, and Fig. 6.7 compares their radiation patterns. All the results of the fine and the coarse model are matched well. Such small errors have no impact on the fabrication so they can be ignored.

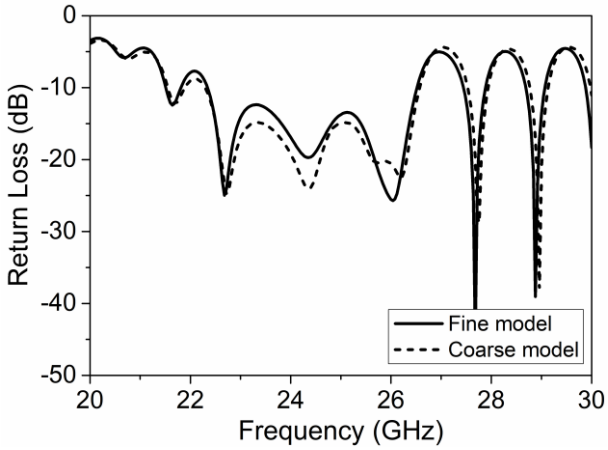


Fig. 6. 5. Simulated return loss of the fine and the coarse model.

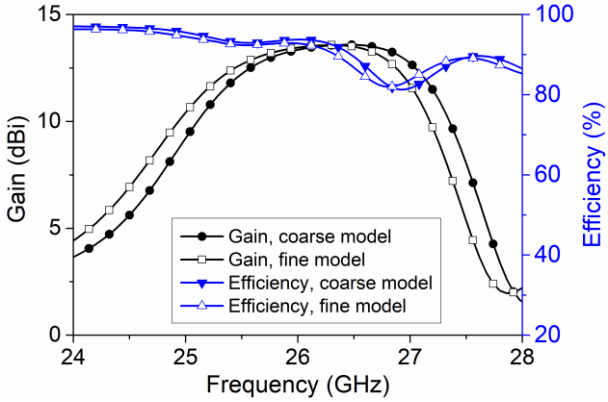


Fig. 6. 6. Simulated gain and efficiency of the fine and the coarse model.

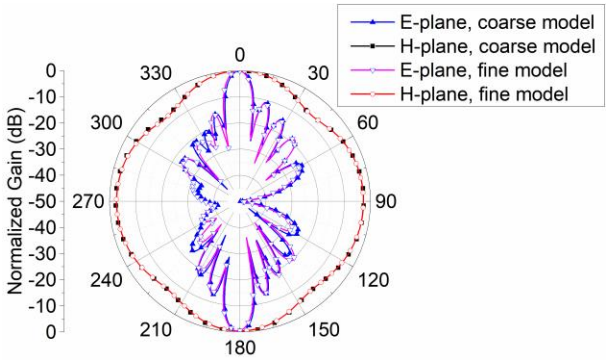


Fig. 6. 7. Simulated normalized radiation patterns of the fine and the coarse model.

### 6.3.2 Fine model simulation and measurement results

Figs. 6.8 - 6.9 present the simulated and measured results of the array. Fig. 6.8 shows that the array has a simulated -10 dB impedance bandwidth of 4.15 GHz (16.8%, 22.56 - 26.71 GHz), while the measured bandwidth is even broader: 6.71 GHz (27.2%, 20.92 - 27.63 GHz). Besides, with a compact size of $5.37\lambda_0 \times 1.04\lambda_0$, the array achieved a high simulated (measured maximum) gain of 13.6 dBi (12.1 dBi) with omnidirectional power radiation at 26 GHz (Fig. 6.9 and Fig. 6.10. a). The curve of the gain (Fig. 6. 9) demonstrated that the array has a flat gain of over 10 dBi in the frequency range of 25 - 27 GHz. Out of this frequency range, however, the feed network cannot provide equiphase power to the dipoles since $L_d$ is no longer equal or close to the guide wavelength. Therefore, the radiation pattern is deformed, and hence, the gain drops out of that frequency range. In addition, the array achieved an average simulated efficiency of over 90% in the frequency range of 24 - 28 GHz. On the other side, the array has, as expected, a simulated (measured) sidelobe level of -13 dB (-11 dB) at H-plane because the elements are uniformly fed. The half-power beam width is $9.86^{o}$ and the cross-polarization levels at both the E- and H-planes are lower than -25 dB.

Therefore, the obtained results have successfully met the specifications set in Chapter 1.

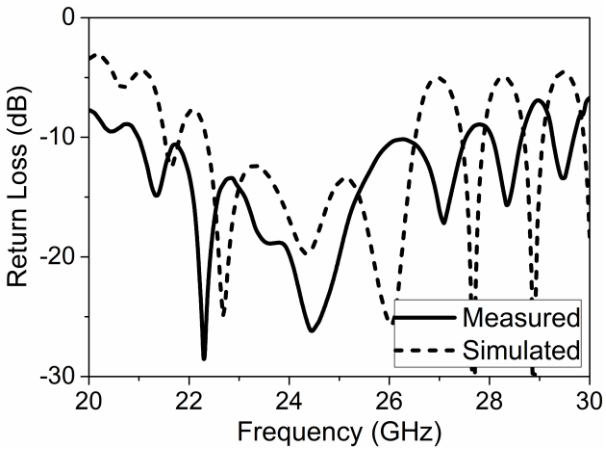


Fig. 6. 8. Simulated and measured return loss of the proposed array.

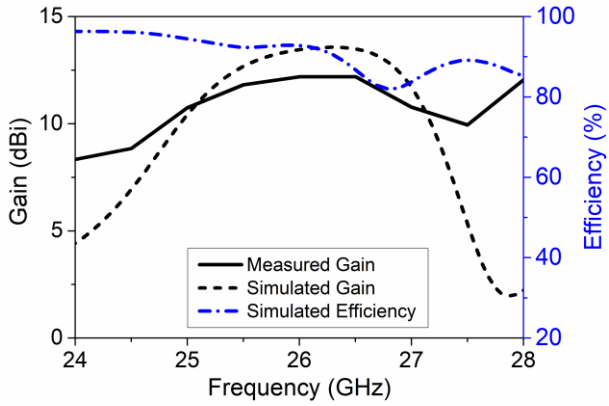


Fig. 6. 9. Simulated and measured maximum gain and efficiency of the proposed array.

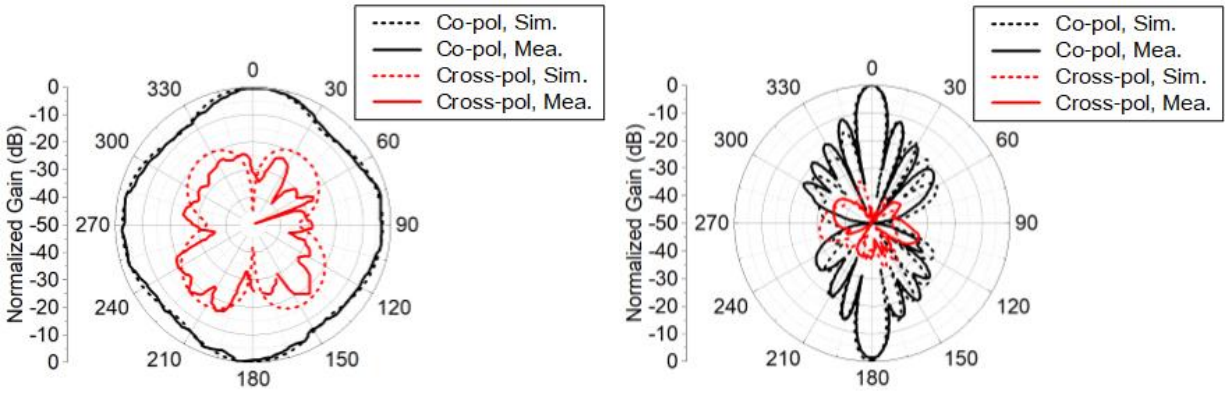


a. b.

Fig. 6. 10. Simulated and measured normalized gain of the proposed array (a. H-Plane, b. E-plane).

## 6.4 Controlling the Directivity of the Array

To complete the design of such an omnidirectional array, we need to know which parameter(s) can influence the directivity. In fact, in this design, the distance between two symmetric dipoles is the major factor that determines the directivity. Fig. 6.11 shows the normalized gain of the array with different values of $L_o$, which reveals that the distance needs to be decreased to get a more omnidirectional pattern. The reason is that this parameter is directedly linked to the H-plane radiation pattern of the antenna element, i.e., the quadrupole.

Not surprisingly, this parameter also influences the return loss, as shown in Fig. 6.12. Therefore, it is quite challenging to find the optimum value of $L_o$. An omnidirectional radiation pattern needs to be achieved, while the return loss cannot exceed -10 dB in the targeted frequency band(s).

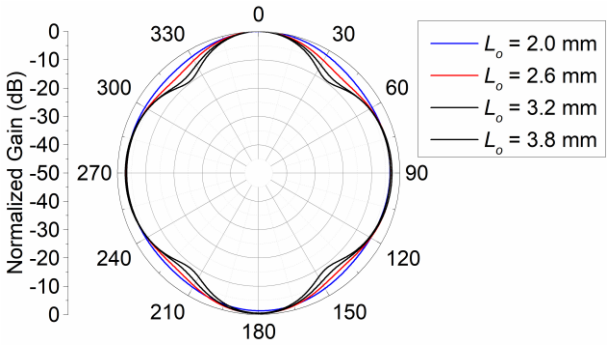


Fig. 6. 11. Simulated normalized gain with various $L_o$ while the other parameters are kept fixed.

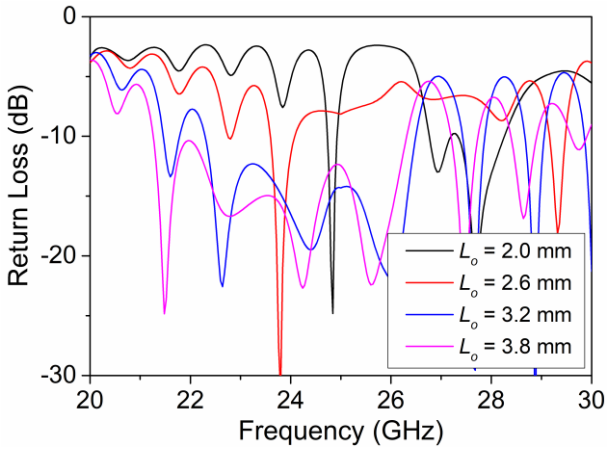


Fig. 6. 12. Simulated return loss with various $L_o$ while the other parameters are kept fixed.

## 6.5 Comparison with Existing Mm-Wave Omnidirectional Antennas and Arrays

As mentioned above, only few mm-wave antenna arrays works have been reported. Table 6.2 compares this work with three existing mm-wave omnidirectional antenna arrays and two antennas. The first four antennas and arrays have been discussed in Section II. To avoid the impact from the connector on the radiation pattern, the size of the prototype fabricated of the array proposed in [7] is in fact around twice of the size presented in the table (around 66×30 mm$^2$). The omnidirectional antenna array discussed in [70] is based on T-slot configuration with a large size while the simulation results showed a moderate performance. By comparison, the array proposed in this paper has a compact size mainly due to its special configuration, which allows the LSIW feed network to be integrated inside of the antenna elements. With a compact size of $5.40\lambda_0 \times 1.04\lambda_0$, it achieved a relative high gain. Furthermore, it exhibits other superior features such as large bandwidth and ease of design/fabrication.

Table. 6. 2 Comparison with Existing mm-wave omnidirectional antennas and Arrays

| Works | Operating Frequency (GHz) | Gain | Sidelobe level | Number of Elements | Dimensions ($mm^2$) | Complexity |
|---|---|---|---|---|---|---|
| [7] (**) | 24.00 - 29.00 (18.8%) | ≈ 11.5 dBi | -15 dB | 8 | 66×15 ($5.72\lambda_0 \times 1.30\lambda_0$) | Moderate |
| [18] (*) | 27.00 – 28.50 (5.4%) | 2.08 dBic | —— | 1 | 3.44×3.44 ($0.32\lambda_0 \times 0.32\lambda_0$) | High |
| [19] (**) | 57.00 - 64.00 (11.6%) | 1.4 dBi | —— | 1 | 4.5×4.3 ($0.91\lambda_0 \times 0.87\lambda_0$) | Low |
| [57] (*) | 25.80 - 29.30 (12.7%) | > 12 dBi | -10 dB | 4 | 68×23.2 ($6.13\lambda_0 \times 2.09\lambda_0$) | Moderate |
| [70] (*) | 27.00 - 29.00 (7.1%) | > 10 dBi | ≈ -11dB | 8 | 100×50 ($9.34\lambda_0 \times 4.67\lambda_0$) | Low |
| **This work (**)** | **21.10 - 27.82 (27.5%)** | **12.3 dBi** | **-11 dB** | **8** | **62×12 ($5.40\lambda_0 \times 1.04\lambda_0$)** | **Low** |

Note: *: Simulated, **: Measured)

## 6.6 Conclusion

In this chapter, a novel printed quadrupole antenna array fed by the LSIW feed network was proposed. A surrogate model was firstly used for modeling and optimization, then a find model was built. The simulated performance of the surrogate coarse model and the fine model were presented for comparison. They were nearly identical as expected. Then, a prototype was fabricated and measured; the measurement results match well with the simulation results. The antenna is omnidirectional. The main factor that influence the radiation pattern was discussed.

The proposed antenna has good performance in terms of bandwidth, gain, and cross-polarization levels. Furthermore, it is low profile, cost-effective, and has simple structure and simple fabrication process. These features were successfully demonstrated by comparison of this work with existing mm-wave omnidirectional antennas and arrays.

# Chapter 7. Conclusion and Future Work

## 7.1 Conclusion

In this research work, an effective approach for SIW device modeling in 3D EM commercial software was proposed. It was demonstrated through the successful design of a novel LSIW series feed network and a mm-wave omnidirectional antenna array with numerous attractive features.

The novel SIW approach was mainly based on existing fundamental theories, highlighting that SIW can be regarded as a normal RWG as long as the design rules are strictly followed. Therefore, a modeling approach using surrogate coarse model for modeling and optimization and fine SIW model for fabrication and measurement was proposed. Such an approach makes the optimization process much more efficient than directly optimizing the fine model. It was validated by four different simulation works namely, a simple SIW, an antenna [57], a novel LSIW feed network, and an array. The simulation results proved that this approach is accurate.

The novel LSIW series feed network was designed to feed quadruple antennas proposed in this work. The SIW-based feed network has one input port and 16 output ports. Simulation results showed that it has very low insertion losses and all the output ports inherently have equiphase power with uniform distribution. The complete design procedure of such a feed network was also presented in this thesis. One can follow the procedure to design a new LSIW feed network easily.

As for the array design, the printed quadrupole antenna was proposed as an antenna array element. This antenna allows the feed network to be integrated inside of it without increasing the overall size of the array. Fed in series by the proposed LSIW feed network, a novel mm-wave omnidirectional antenna array was then constructed. The array exhibits several attractive features such as broad bandwidth and high gain. The array can radiate power omnidirectionally due primarily to the quadrupole configuration and the proposed LSIW feed network.

The proposed array was simulated, fabricated, and tested. Both the simulated and measured results demonstrated that the omnidirectional array has good performance in terms of impedance bandwidth, gain, efficiency, and cross-polarization level. Besides, the array offers some other attractive features like low profile, low cost, compactness, simple fabrication process, etc., making it a suitable candidate for future mm-wave communication systems.

## 7.2 Future Work

Based on the current research work, some other novel antennas and feed networks could be designed.

At first, more rules for directly converting the SIW coarse model to a fine model are necessary. This can be done with more experimental data and some numerical analysis technique.

Secondly, omnidirectional antenna arrays with a similar configuration but with more elements can be designed. In fact, designing an array with even higher gain is, theoretically, possible. But this should be constrained by the increased physical size of the array to be designed. An advantage of such an array is its very low losses due to the low loss LSIW feed network, as discussed in Chapter 5. This is, in fact, one of the attractive features of SIW. However, low losses do not mean no losses. When the physical size of the LSIW increase, the losses will also be increased. So, infinitely increasing the number of elements will not infinitely increasing the gain of the array designed. Therefore, following the design procedure to design a 1×16 or 1×32 array is feasible.

On the other side, the LSIW feed network proposed in this research work has proved that designing series feed networks (power splitters) is possible. Keeping the output ports on one side while deleting the output ports on the other side can form a simple LSIW series power splitter. Such a power splitter is suitable to feed narrowband antenna arrays. For broadband antenna arrays, however, this kind of feed network is no longer suitable since it cannot provide equiphase power in a wide frequency range. An alternative solution should be proposed. This is, therefore, a direction to explore in order to design broadband devices.

Furthermore, new types of arrays can be explored based on the LSIW feed network since the feed network offers low loss performance, which is greatly desired for antennas. The feed network used can directly affect the performance of the array to be designed. Using the same feed network, some other types of antenna element such as patch antennas can be investigated. Such a feed network can also be combined with a SIW parallel feed network to build a planar microstrip patch antenna array.

In fact, several novel designs can be explored thanks to the proposed LSIW feed network and array.

# References


[1] http://www.idc-online.com/technical_references/pdfs/electronic_engineering/Antenna_Fundamentals.pdf, last access April 10, 2021.

[2] J. Zhang, X. Ge, Q. Li, M. Guizani, and Y. Zhang, "5G millimeter-wave antenna array: design and challenges," *IEEE Wireless Commun.*, vol. 24, pp. 106-112, Apr.2017.

[3] G. Destino and H. Wymeersch, "On the trade-off between positioning and data rate for mm-wave communication," in *IEEE Int. Conf. on Commun. Workshops*, pp. 797-802, Paris, France, May 2017.

[4] N. Garcia, H. Wymeersch, E.G. Ström, and D. Slock, "Location-aided mm-wave channel estimation for vehicular communication," in *IEEE Int. Workshop on Signal Processing Advances in Wireless Commun.*, pp. 1-5, Edinburgh, UK, July 2016.

[5] T.S. Rappaport et al., "Millimeter wave mobile communications for 5G cellular: It will work!" *IEEE Access*, vol. 1, pp. 335-349, May 2013.

[6] M.J. Marcus, "5G and 'IMT for 2020 and beyond' [spectrum policy and regulatory issues]," *IEEE Wireless Commun.*, vol. 22, pp. 2-3, Aug. 2015.

[7] C.X. Mao, M. Khalily, P. Xiao, T.W.C. Brown, and S. Gao, "Planar sub-millimeter-wave array antenna with enhanced gain and reduced sidelobes for 5G broadcast applications," *IEEE Trans. Antennas Propag.*, vol. 67, pp. 160-168, Oct. 2018.

[8] W.L. Stutzman and G.A. Thiele, *Antenna Theory and Design*. 3rd Ed., J. Wiley & Sons, 2012, pp. 109.

[9] S. Rangan, T.S. Rappaport, and E. Erkip, "Millimeter-wave cellular wireless networks: potentials and challenges," *Proc. IEEE*, vol. 102, pp. 366-385, Mar. 2014.

[10] A. Petosa, "Course Notes for ELEC 5607 Fundamentals of Antenna Engineering", Carleton University, Ottawa, unpublished.

[11] D. Basu, *Dictionary of Pure and Applied Physics*. 2nd Ed., New York: CRC Press, 2001, pp. 21.

[12] Y. Fan, X. Liu, B. Liu, and R. Li, "A broadband dual-polarized omnidirectional antenna based on orthogonal dipoles," *IEEE Antennas Wireless Propag. Lett.*, vol. 15, pp. 1257-1260, Nov. 2015.

[13] X. Dai, Z. Wang, C. Liang, X. Chen, and L. Wang, "Multiband and dual-polarized omnidirectional antenna for 2G/3G/LTE application," *IEEE Antennas Wireless Propag. Lett.*, vol. 12, pp. 1492-1495, Nov. 2013.

[14] B. Li and Q. Xue, "Polarization-reconfigurable omnidirectional antenna combining dipole and loop radiators," *IEEE Antennas Wireless Propag. Lett.*, vol. 12, pp. 1102-1105, Sept. 2013.

[15] X. Cai and K. Sarabandi, "A compact broadband horizontally polarized omnidirectional antenna using planar folded dipole elements," *IEEE Trans. Antennas and Propag.*, vol. 64, pp. 414-422, Feb. 2016.

[16] K. Sellal and L. Talbi, "Design of a two-element antenna array using substrate integrated waveguide technique," *Int. J. of Microwave Science and Tech.*, vol. 2011, pp. 1-7, Aug. 2011.

[17] N.O. Parchin, M. Shen, and G.F. Pedersen, "UWB MM-wave antenna array with quasi omnidirectional beams for 5G handheld devices," in *IEEE Int. Conf. Ubiquitous Wireless Broadband*, pp. 1-4, Nanjing, China, Oct. 2016.

[18] W. Lin and R. Ziolkowski, "Compact, omni-directional, circularly-polarized mm-Wave antenna for device-to-device (D2D) communications in future 5G cellular systems," in *Global Symp. on Millimeter-Waves*, pp. 115-116, Hong Kong, China, May 2017.

[19] S. Ranvier et al., "Low-Cost Planar Omnidirectional Antenna for mm-Wave Applications," *IEEE Antennas and Wireless Propag. Lett.*, vol. 7, pp. 521-523, Aug. 2008.

[20] J. Hirokawa and M. Ando, "Single-layer feed waveguide consisting of posts for plane TEM wave excitation in parallel plates," *IEEE Trans. Antennas and Propag.*, vol. 46, pp. 625-630, May 1998.

[21] J. Xu, Z.N. Chen, and X. Qing, "CPW Center-Fed Single-Layer SIW Slot Antenna Array for Automotive Radars," *IEEE Trans. Antennas and Propag.*, vol. 62, no. 9, pp. 4528-4536, Sept. 2014.

[22] L. Sabri, N. Amiri, and K. Forooraghi, "Dual-Band and Dual-Polarized SIW-Fed Microstrip Patch Antenna," *IEEE Antennas and Wireless Propag. Lett.*, vol. 13, pp. 1605-1608, July 2014.

[23] B. Potelon, J. Favennec, C. Quendo, E. Rius, C. Person, and J. Bohorquez, "Design of a Substrate Integrated Waveguide (SIW) Filter Using a Novel Topology of Coupling," *IEEE Microw. Wireless Compon. Lett.*, vol. 18, no. 9, pp. 596-598, Sept. 2008.

[24] J. Xu, Z.N. Chen, X. Qing, and W. Hong, "140-GHz Planar Broadband LTCC SIW Slot Antenna Array," *IEEE Trans. Antennas and Propag.*, vol. 60, pp. 3025-3028, June 2012.

[25] K. Fan, Z. Hao, Q. Yuan, J. Hu, G. Q. Luo, and W. Hong, "Wideband horizontally polarized omnidirectional antenna with a conical beam for millimeter-wave applications," *IEEE Trans. Antennas and Propag.*, vol. 66, pp. 4437-4448, Sept. 2018.

[26] K. Sarhadi and M. Shahabadi, "Wideband substrate integrated waveguide power splitter with high isolation," *IET Microwaves, Antennas & Propag.*, vol. 4, pp. 817-821, July 2010.

[27] S. Park, D. Shin, and S. Park, "Low side-lobe substrate-integrated-waveguide antenna array using broadband unequal feeding network for millimeter-wave handset device," *IEEE Trans. Antennas and Propag.*, vol. 64, pp. 923-932, Mar. 2016.

[28] C. A. Balanis, *Antenna Theory, Analysis and Design*, John Wiley & Sons, Inc., 2nd ed. 1982.

[29] https://en.wikipedia.org/wiki/Bandwidth_(signal_processing), last access April 10, 2021.

[30] Y. Cassivi, L. Perregrini, P. Arcioni, M. Bressan, K. Wu, and G. Conciauro, "Dispersion characteristics of substrate integrated rectangular waveguide," *IEEE Microw. Wireless Compon. Lett.*, vol. 12, pp.333–335, Sept. 2001.

[31] J.E. Rayas-Sanchez and V. Gutierrez-Ayala, "A general EM-based design procedure for single-layer substrate integrated waveguide interconnects with microstrip transitions," in *IEEE MTT-S Int. Microwave Symp.*, pp. 983-986, Atlanta, USA, June 2008.

[32] D. Deslandes, "Design equations for tapered microstrip-to-Substrate Integrated Waveguide transitions," in *IEEE MTT-S Int. Microwave Symp.*, pp. 704-707, Anaheim, USA, May 2010.

[33] Ansys® High Frequency Structure Simulator, Release 19.1.

[34] CST Studio Suite, "CST Microwave Studio," http:// www.cst.com

[35] B. Potelon, J. Favennec, C. Quendo, E. Rius, C. Person, and J. Bohorquez, "Design of a Substrate Integrated Waveguide (SIW) Filter Using a Novel Topology of Coupling," *IEEE Microwave Wireless Compon. Lett.*, vol. 18, no. 9, pp. 596-598, Sept. 2008.

[36] K. Sarhadi and M. Shahabadi, "Wideband substrate integrated waveguide power splitter with high isolation," *IET Microwaves, Antennas & Propag.*, vol. 4, pp. 817-821, July 2010.

[37] H. Wang, D.G. Fang, B. Zhang, and W.Q. Chen, "Dielectric Loaded Substrate Integrated Waveguide (SIW) -Plane Horn Antennas," *IEEE Trans. Antennas and Propag.*, vol. 58, no. 3, pp. 640-647, Mar. 2010.

[38] http://www.ee.bilkent.edu.tr/~microwave/programs/magnetic/rect/info.htm, last access April 10, 2021.

[39] https://www.everythingrf.com/tech-resources/waveguides-sizes, last access April 10, 2021.

[40] D. Deslandes and K. Wu, "Integrated microstrip and rectangular waveguide in planar form," *IEEE Microwave Wireless Compon. Lett.*, vol. 11, no. 2, pp. 68-70, Feb. 2001.

[41] B.N. Das, K.V.S.V.R. Prasad, and K.V.S. Rao, "Excitation of Waveguide by Stripline- and Microstrip-Line-Fed Slots," *IEEE Trans. Microwave Theory Tech.*, vol. 34, no. 3, pp. 321-327, Mar 1986.

[42] W. Grabherr, W.G.B. Huder, and W. Menzel, "Microstrip to waveguide transition compatible with MM-wave integrated circuits," *IEEE Trans. Microwave Theory Tech.*, vol. 42, no. 9, pp. 1842-1843, Sept. 1994.

[43] T.Q. Ho, Y.-C. Shih, and Yi-Chi Shih, "Spectral-domain analysis of E-plane waveguide to microstrip transitions," *IEEE Trans. Microwave Theory Tech.*, vol. 37, no. 2, pp. 388-392, Feb. 1989.

[44] L.J. Lavedan, "Design of waveguide-to-microstrip transitions specially suited to millimeter-wave applications," *Electron. Lett.*, vol. 13, no. 20, pp. 604-605, Sept. 1977.

[45] F. Shigeki, "Waveguide line," (in Japanese) Japan Patent 06-053 711, Feb. 25, 1994.

[46] J. Hirokawa and M. Ando, "Single-layer feed waveguide consisting of posts for plane TEM wave excitation in parallel plates," *IEEE Trans. Antennas Propag.*, vol. 46, no. 5, pp. 625–630, May 1998.

[47] A. Zeid and H. Baudrand, "Electromagnetic scattering by metallic holes and its applications in microwave circuit design," *IEEE Trans. Microw. Theory Tech.*, vol. 50, no. 4, pp. 1198–1206, Apr. 2002.

[48] D. Deslande and K. Wu, "Single-substrate integration technique of planar circuits and waveguide filters," *IEEE Trans. Microw. Theory Tech.*, vol. 51, no. 2, pp. 593–596, Feb. 2003.

[49] F. Xu and K. Wu, "Guided-wave and leakage characteristics of substrate integrated waveguide," *IEEE Trans. Microwave Theory Tech.*, vol. 53, pp. 66-73, Jan. 2005.

[50] T. Vu Khac and C. Carson, "Impedance properties of a longitudinal slot antenna in the broad face of a rectangular waveguide," *IEEE Trans. Antennas Propag.*, vol. 21, no. 5, pp. 708-710, Sept. 1973.

[51] A. U. Zaman and P. Kildal, "Wide-band slot antenna arrays with single-layer corporate-feed network in ridge gap waveguide technology," *IEEE Trans. Antennas Propag.*, vol. 62, no. 6, pp. 2992-3001, June 2014.

[52] D. Stephens, P.R. Young, and I.D. Robertson, "W-band substrate integrated waveguide slot antenna," *Electronics Lett.*, vol. 41, no. 4, pp. 165-167, Feb. 2005.

[53] J.E. Rayas-Sanchez and V. Gutierrez-Ayala, "A general EM-based design procedure for single-layer substrate integrated waveguide interconnects with microstrip transitions," in *IEEE MTT-S Int. Microwave Symp.*, pp. 983-986, Atlanta, USA, June 2008.

[54] D. Deslandes and K. Wu, "Design consideration and performance analysis of substrate integrated waveguide components," in European Microwave Conf, pp. 881-884, Milan, Italy, Mar. 2002.

[55] Y. Cassivi, L. Perregrini, P. Arcioni, M. Bressan, K. Wu, and G. Conciauro, "Dispersion characteristics of substrate integrated rectangular waveguide," *IEEE Microwave Wireless Compon. Lett.*, vol. 12, no. 9, pp. 333-335, Sept. 2002.

[56] V. K. Devabhaktuni, M.C.E. Yagoub, and Q. J. Zhang, "A robust algorithm for automatic development of neural-network models for microwave applications," *IEEE Trans. Microw. Theory Techn.*, vol. 49, no. 12, pp. 2282-2291, Dec. 2001.

[57] Y. Liu, M.C.E. Yagoub, and M. Nassor, "Omni-directional antenna array with improved gain for 5G communication systems," in *IEEE Int. Symp. Antennas Propag. and North American Radio Science Meeting*, Montreal, Canada, July 2020.

[58] X. P. Chen and K. Wu, "Substrate integrated waveguide filter with improved stopband performance for satellite ground terminal," *IEEE Trans. Microw. Theory Techn.*, vol. 57, no. 3, pp. 674-683, Mar. 2009.

[59] D. Deslandes and K. Wu, “Analysis and design of current probe transition from grounded coplanar to substrate integrated rectangular waveguides,” *IEEE Trans. Microwave Theory Tech.*, vol. 53, pp. 2487-2494, Aug. 2005.

[60] N. Jain and N. Kinayman, “A novel microstrip mode to waveguide mode transformer and its applications,” in *IEEE MTT-S Int. Microwave Symp.*, vol. 2, pp. 623-626, Phoenix, USA, May 2001.

[61] D. Deslandes, “Design equations for tapered microstrip-to-Substrate Integrated Waveguide transitions,” in *IEEE MTT-S Int. Microwave Symp.*, pp. 704-707, Anaheim, USA, May 2010.

[62] N. Kaneda, W.R. Deal, Yongxi Qian, R. Waterhouse, and T. Itoh, “A broadband planar quasi-Yagi antenna,” *IEEE Trans. Antennas Propag.*, vol. 50, no. 8, pp. 1158-1160, Aug. 2002.

[63] H.K. Kan, R.B. Waterhouse, A.M. Abbosh, and M.E. Bialkowski, "Simple broadband planar CPW-fed quasi-Yagi antenna," *IEEE Antennas and Wireless Propag. Lett.*, vol. 6, pp. 18-20, July 2007.

[64] G. Bai, Y. Liu, and C. Liao, “A broad band high gain microstrip Yagi antenna array for mm-wave communication systems. in *Int. Conf. on Radar, Antenna, Microwave, Electronics and Telecomm., pp. 180-183, Tangerang, Indonesia*, Nov. 2020.

[65] S. A. Rezaeieh, M. A. Antoniades and A. M. Abbosh, “Miniaturized planar Yagi antenna utilizing capacitively coupled folded reflector,” *IEEE Antennas and Wireless Propag. Lett.*, vol. 16, pp. 1977-1980, Apr. 2017.

[66] Y. Liu and M.C.E. Yagoub, “Compact, broadband, and omnidirectional antenna array for millimeter-wave communication systems”, *Journal of Microwaves, Optoelectronics and Electromagnetic Applications*, vol. 20, no. 2, pp. 297–306, Apr. 2021.

[67] Z.C. Hao, W. Hong, H. Li, H. Zhang, and K. Wu, “Multiway broadband substrate integrated waveguide (SIW) power divider,” in *IEEE Antennas and Propag. Society Int. Symp.*, pp. 639-642, Washington, USA, July 2005.

[68] W. Mazhar, D. Klymyshyn, and A. Qureshi, “Design and analysis of wideband eight-way SIW power splitter for mm-wave applications,” *Int. J. RF Microw. Comput.-Aided Eng.*, vol. 28, no. 2, Nov. 2017, Art. no. e21196.

[69] Y. Yan, I. Chen, C. Peng, and W. Lin, “A compact 8-way power divider,” in *IEEE 5th Asia-Pacific Conf. Antennas and Propag.*, pp. 213-214, Kaohsiung, Taiwan, July 2016.

[70] A. Zhao and F. Ai, “5G mm-wave antenna array based on T-slot antenna for mobile terminals,” in *IEEE Asia-Pacific Conf. on Antennas and Propag.*, pp. 476-477, Auckland, New Zealand, Aug. 2018.